Draft version November 4, 2021
Typeset using LaTeX **twocolumn** style in AASTeX63

The far ultra-violet background

S. R. Kulkarni[1]

[1] *Owens Valley Radio Observatory 249-17, Caltech*
Pasadena, CA 91125, USA

Submitted to PASP

ABSTRACT

The diffuse far-ultraviolet (FUV) background has received considerable attention from astronomers since the seventies. The initial impetus came from the hope of detecting UV radiation from the hot intergalactic medium. The central importance of the FUV background to the physics (heating and ionization) of the diffuse atomic phases motivated the next generation of experiments. The consensus view is that the diffuse FUV emission at high latitudes has three components: stellar FUV reflected by dust grains (diffuse galactic light or DGL), FUV from other galaxies (extra-galactic background light, EBL) and a component of unknown origin (and referred to as the "offset" component). During the eighties, there was some discussion that decaying dark matter particles produced FUV radiation. In this paper I investigate production of FUV photons by conventional sources: line emission from Galactic Hot Ionized Medium, two-photon emission from the Galactic Warm Ionized Medium and low-velocity shocks, and Lyman-β fluorescence of hydrogen at several locales in the Solar System (the interplanetary medium, the exosphere and thermosphere of Earth). I conclude that two thirds and arguably all of the offset component can be explained by the sum of the radiation from the processes listed above.

1. BACKGROUND

The diffuse background in the wavelength range 912–2000 Å is of central importance to the physics of the diffuse atomic phases – the Cold Neutral Medium (CNM) and the Warm Neutral Medium (WNM). Even though historically, the various bands of ultra-violet (UV) were defined by wavelength properties of detectors and mirror coatings, here, following *GALEX*, we use the term Far-Ultraviolet (FUV) band for the wavelength range 1350–1750 Å.

The diffuse FUV radiation, via photo-electric ionization of C I and photo-electric heating of dust particles, heats the two atomic phases mentioned above. The same radiation, via ionization of elements with ionization potential less than that of hydrogen, also provides residual ionization to the two atomic phases. The FUV background is of importance for the molecular medium also. FUV photons excite the Lyman and Werner bands of H_2 (Duley & Williams 1980) which result in UV fluorescent line emission and once in ten times leads to dissociations (Jura 1974; Draine & Bertoldi 1996). In the process, the strength of FUV radiation determines the transition in diffuse clouds between atomic and molecular phases.

Separately, scattering of solar photons by zodiacal dust particles constitute an irreducible background for space missions located in the inner Solar system, e.g., the Hubble Space Telescope (HST) in low earth orbit (LEO) or the planned Russian Spektr-UF mission (aka "World Space Observatory" or WSO) which, like the pioneering International Ultraviolet Observatory, is expected to be in a geo-synchronous orbit (GEO; Boyarchuk et al. 2016) and thereby avoid strong oxygen lines, endemic to LEO missions. However, the Sun is faint in the FUV. Ergo, the sky is dark in the FUV band. As a result, the FUV band is most attractive for low surface brightness imaging of galaxies (O'Connell 1987). Indeed, it is precisely this advantage of the FUV band that allowed *GALEX* to discover very faint star-forming complexes well beyond the optical disk and with sensitivity better than that provided by ground-based Hα imaging (e.g., Barnes et al. 2011).

In the late sixties it was speculated that the hot intergalactic medium (IGM) would be revealed by diffuse FUV emission. Searches for diffuse UV emission were

Corresponding author: S. R. Kulkarni
srk@astro.caltech.edu

undertaken with great gusto. Good summaries of the first two decades of this period can be found in Kurt & Sunyaev (1970), Paresce & Jakobsen (1980) and Henry (1991). Separately, this was also the period when the first pulsar surveys showed that pulsar signals were invariably dispersed (see, for example, Manchester & Taylor 1977; Yao et al. 2017). As a result, astronomers became aware of a pervasive Galactic ionized medium. During the eighties, thanks primarily to the work of Ronald J. Reynolds, this ionized medium was complementarily sensed via Hα recombination emission (see Haffner et al. 2009). These two methods – dispersion of radio signals and diffuse Hα emission – led to the recognition of the Warm Ionized Medium (WIM) as a distinct phase of the ISM.

The filling factor of the WIM, by volume, is estimated to be between 20% and 40% of the Galactic disk (Haffner et al. 2009). The ionizing power requirement for the WIM is tremendous. The conventional explanation required a significant fraction of Lyman continuum photons from OB stars (Reynolds 1990) and also called for a porous ISM so as to allow for Lyman continuum photons to travel significantly away from their parent stars. The observed large vertical scale height, ≈ 1 kpc, of the WIM was initially a mystery. This "crisis" led to a resurrection of a hypothesis of decaying dark matter as a major source of ionizing photons (Stecker 1980; Sciama 1990; more recent references include Kollmeier et al. 2014; Henry et al. 2015). Miller & Cox (1993) and Dove & Shull (1994) provided a conventional explanation based on O stars as the principal source of ionizing radiation, radiative transfer modeling and clustering of star-forming regions, "chimneys" and "channels" while Slavin et al. (2000) made a strong case for (high latitude) ionizing radiation resulting from old supernova remnants.

The study of diffuse FUV radiation continued through the nineties with rocket-borne experiments, UV spectrometers on Voyager missions, Shuttle-based experiments, FAUST and FUSE. Murthy et al. (2019) provide a comprehensive list of FUV experiments. Two missions, both launched in 2003, greatly advanced the field of diffuse FUV radiation: *GALEX* (Martin et al. 2005) carrying both an FUV and a near-UV (NUV; 1750–2800 Å) wide-field imager, each with a field-of-view (FoV) of over a square degree but with pixel size of only a few arc-seconds. STSAT-1 carrying the Far-UV Imaging Spectrometer (FIMS[1]; Edelstein et al. 2006) undertook spectral (900–1750 Å) imaging of the sky. The resulting data provide key information of the physical parameters of the Galactic Hot Ionized Medium (HIM) as well as pin-pointing sites of molecular fluorescence.

The consensus from all these studies is that much of the diffuse FUV emission is due to reflection of stellar FUV photons by diffuse ("cirrus") clouds and conveniently traced by IRAS 100 μm band or fluorescence of stellar FUV photons by molecular hydrogen. Together this emission is called as the Diffuse Galactic Light (DGL). However, some diffuse background emission is *not* correlated with cirrus clouds, a fraction of which can be reasonably attributed to collective emission from other galaxies – the so-called Extragalactic Background Light (EBL). There remains some 120–180 CU emission in the FUV band which cannot be attributed to either DGL or EBL and was given the name "offset" component.[2] Here, CU ("continuum unit") stands for photon cm^{-2} s^{-1} Å^{-1} sr^{-1} with "sr" as a short for steradian. A related unit is "line unit" (LU) which stands for photon cm^{-2} s^{-1} sr^{-1}. We take the occasion to introduce "Rayleigh" (R) which is a unit for surface brightness of line emission and routinely used in aeronomy. Numerically, one Rayleigh is $10^6/(4\pi)$ photon cm^{-2} s^{-1} sr^{-1}. Thus $1\,R \approx 79,577$ LU.

The purpose of this paper is to investigate possible origin(s) for this offset component. The paper is organized as follows. In §2 we review the measurements of diffuse high-latitude FUV emission. This is followed by a summary of the essential physics of hydrogen two-photon decay (§3). We investigate contribution to the FUV band from conventional sources: line emission from the Galactic HIM, two-photon emission from the Galactic WIM and low-velocity shocks (§4) and two photon-photon continuum arising from fluorescence of Lyβ excitation (§5) in the Solar System: the Interplanetary Medium[3] (§6), the Earth's atmosphere ("thermosphere"; §7) and the exosphere (§8). In §9 we tally the contributions to the diffuse FUV background and conclude that about two thirds of the diffuse FUV background can be accounted for by contributions discussed in §4-8. We conclude in §10.

2. THE DIFFUSE FUV EMISSION

[1] also sometimes referred to as SPEAR

[2] DGL is proportional to the column density of dust. However, this linear relation has an offset: radiation even when the dust column is very low – hence the name "offset".

[3] The term IPM has two different connotations in astronomy. In radio astronomy, IPM refers to the solar wind that pervades the solar system out to the heliopause. In planetary studies, the IPM stands for the very local interstellar cloud into which the Solar system is moving.

The "Interstellar Radiation Field" (ISRF), being a central quantity, is almost assured of a chapter in any book on the ISM (e.g., Chapter 12, Draine 2011). The ISRF is composed of both resolved (bright) stars and diffuse emission. Only the latter component is of interest to this paper. There have been extensive reviews of the diffuse FUV emission (e.g. see Paresce et al. 1980; Henry 1991; Henry et al. 2015). Here we focus on the measurements of the diffuse FUV by *GALEX*.

GALEX was well suited to measuring the diffuse UV emission because its FUV and NUV imagers not only had good angular resolution (few arc-seconds) but also a large FoV. This resolution allowed for masking out point sources and galaxies. The resulting ten-year trove of data was well suited to discerning the diffuse background. *GALEX* was in LEO with an orbital period of 99 minutes. To minimize airglow, observations were restricted to narrow periods lasting only 25–30 minutes during Earth eclipse (Morrissey et al. 2007).

We refer to two major studies of diffuse FUV carried out with *GALEX*: one led by Jayant Murthy and associates (e.g., Murthy et al. 2010; Akshaya et al. 2019) and the other, the PhD thesis of Erika Hamden (Hamden et al. 2013). These papers provide an excellent summary of past efforts to measure the diffuse FUV emission at high Galactic latitudes. The conclusions from these studies are largely concordant and briefly are as follows:

1. At mid to high Galactic latitudes, the FUV intensity scales linearly with the IRAS 100 μm intensity up to an intensity of 8 MJy sr^{-1} (e.g., Seon et al. 2011). This is attributed to reflection of stellar FUV photons from hot stars (primarily located in the Galactic plane) by interstellar dust. The same dust particles, heated by stellar light (including the FUV), radiate at long wavelengths and produce the IRAS 100 μm band, hence the correlation.The FUV emission saturates at higher values of 100 μm emission presumably because the absorption of the FUV radiation by the clouds outweighs over reflection.

2. The FUV intensity increases in the direction of interstellar clouds which harbor molecular hydrogen. This is attributed to fluorescence by photons in the Lyman band (912–1216 Å) and FUV photons (see Martin et al. 1990; Jo et al. 2017). The reflected and the fluorescent components are the primary contributors to DGL.

3. At high Galactic latitudes, diffuse FUV background is present, even in directions towards dust-free regions. Only about half of the emission can be reasonably attributed to emission from other galaxies, the EBL.

   Hamden et al. (2013) conclude "*There is a* $\sim$ 300 *CU FUV isotropic offset which is likely due to a combination of air glow (probably the dominant contributor), a small extragalactic background component including continuum light from unresolved galaxies, and/or a Galactic component not traced by other indicators*". Akshaya et al. (2018) state "*There is an excess emission (over the DGL and the EBL) of 120–180 photon units*[4] *in the FUV and 300–400 photon units in the NUV ... Although we do not know its origin, we can affirm that the excess emission cannot be accounted for by current models of the DGL and EBL.*"

The goal of this paper is investigation of the emission discussed in item (3) above. This emission is referred to as "offset" or "offset/isotropic". We do not consider the isotropic nature to be firmly established since the primary observation is principally from high latitude regions. Below we investigate conventional processes which generate FUV photons. Only if the totality of the surface brightness produced by these processes fail to account for the offset emission would it be logical to pursue increasingly exotic explanations.

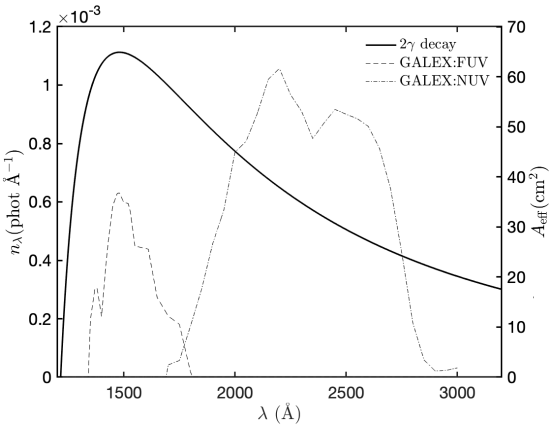

Figure 1. (Left y axis): The photon spectrum of a single two-photon decay, n_λ (solid line) as a function of the wavelength, λ. Since each decay leads to emission of two photons, $\int n_\lambda d\lambda = 2$. (Right y axis): Effective area of *GALEX* FUV and NUV bands as a function of λ (dot-dash and dashed lines). The details of the fitting formula used to generate the two-photon decay spectrum and effective area of *GALEX* can be found in §A.

3. TWO-PHOTON DECAY

[4] The "photon unit" discussed here is the same as CU.

A low density astrophysical plasma which is in collisional ionization equilibrium (CIE), and with sufficient column density to be in "case B"[5] and at a temperature $\lesssim 50,000$ K, cools via Lyα, two-photon continuum, free-bound radiation and optical/IR recombination lines (e.g., Hα). Lyα photons undergo many scatterings, ending their life upon encountering dust particles within or close to its birth site (see, Neufeld 1990; Seon et al. 2021). In contrast, two-photon continuum and recombination radiation freely escape. Separately, H atom can be excited by Lyman line photons and two-photon continuum emitted as the excited atoms relax to the ground state ("fluorescence").

An H atom which finds itself in a 2s level will, if undisturbed by a collision, radiatively decay by emitting two photons over a timescale of $A_{2\gamma}^{-1} \approx (8.2\,\mathrm{s}^{-1})^{-1}$; see Figure 1. The sum of the energies of the two photons is equal to that of Lyα or 10.2 eV. The two-photon continuum (and associated Hα) escape freely and can contribute to the FUV background. The factors to convert the two-photon spectrum to FUV and NUV counting rates are central to this paper and a full discussion can be found in §A. The key result is the following: 10^6 two-photon decays cm^{-2} s^{-1} results in 85.1 CU in the FUV channel and 18.4 CU in the NUV channel (Table 3).

4. THE GALAXY

The reader is advised to consult Draine (2011) for a description of the three primary atomic phases; the WNM, WIM and HIM. Locally, the WNM, the WIM and the HIM occupy most of the interstellar space (Cox 2005). While the WIM contributes to the FUV band by two-photon emission, the HIM primarily contributes to the FUV background via line emission. Separately, it turns out that low-velocity shocks are also emitters of two-photon continuum. Below we discuss the various contribution to the FUV background from these three Galactic sources.

4.1. *The Warm Ionized Medium*

Deharveng et al. (1982) investigated two-photon emission from the WIM and concluded that it could not account for the FUV background. Martin et al. (1991), Reynolds (1992) and Seon et al. (2011) came to similar conclusions. Rather than compute the expected two-photon emission from the physical parameters of the WIM (as was done in the past papers) we prefer the simpler approach of estimating the two-photon brightness directly from observations of Hα. At the temperature of the WIM (8,000 K), assuming case B, we expect that for every two-photon decay there are 1.47 Hα photons.

In Figure 2 we display the histogram of Galactic Hα surface brightness as recorded in the Wisconsin Hα Mapper Sky Survey (WHAM-SS or WHAM for short; Haffner et al. 2003, 2010). From these figures we conclude that the Galactic Hα emission towards the Galactic polar cap is approximately 0.5 R. We subtract 20% to account for contribution resulting from scattering of Hα emission by cirrus clouds (Witt et al. 2010; Dong & Draine 2011). The expected two-photon decay rate is then $0.27\,R$ which corresponds to 22.7 CU in the FUV band.

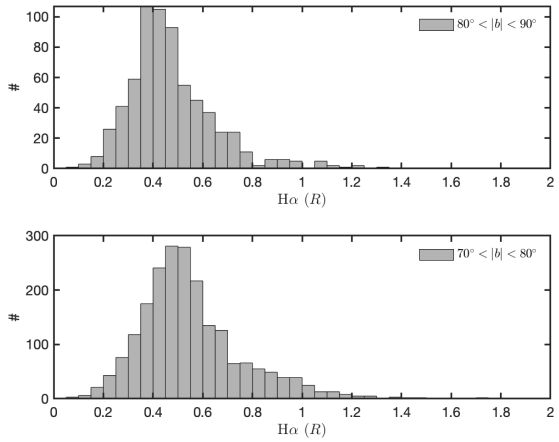

Figure 2. Histogram of the WHAM Hα brightness towards the Galactic caps. The vertical-axis refers to the number of WHAM beams. Data obtained from WHAM. The size of the WHAM beam is about a degree. (Haffner et al. 2003, 2010).

4.2. *The Hot Ionized Medium*

The three dominant metals have strong resonance lines (2s→2p) in the UV, which conveniently probe a range of temperatures (Sutherland & Dopita 1993): CIV ($\lambda\lambda$ 1548.2, 1550.8 Å; 1×10^5 K), NV ($\lambda\lambda$ 1242.8, 1238.8 Å; 2×10^5 K) and OVI ($\lambda\lambda$ 1037.6, 1031.9 Å; 3×10^5 K). FUSE observations of OVI established the presence of widespread HIM in the halo of the Galaxy (Savage et al. 2000) and in the disk of the Galaxy (Bowen et al. 2008).

FIMS/SPEAR aboard South Korea's STSAT-1 satellite undertook all sky spectral-imaging in the wavelength range 900–1150 Å and 1350–1750 Å (Seon et al. 2011; Jo et al. 2017, 2019). The authors fit high latitude data to a CIE model and find a plasma temperature of 2×10^5 K and a vertical emission measure of $\int n_e(z)^2 dz$ of 0.01 cm^{-6} pc. For these parameters, the free-free emission amounts to < 1 CU in the FUV band. The most prominent line in the spectrum towards the Galac-

[5] Regions which are thick to Lyman continuum photons are in case B.

tic poles is the CIV doublet with a strength of 4,600 LU. Separately, Martin et al. (1991) report a similar detection towards the Lockman hole – a region with a very low (lowest?) H I column density. We will thus assume that 4,600 LU is not reflected light but is genuine emission from high-latitude HIM.

In order to determine the total emission from the HIM we need to account for fainter lines and continuum (free-bound, primarily). To this end, we used CHIANTI (Dere et al. 1997; Del Zanna et al. 2021) and obtained the CIE spectrum of a solar-abundance plasma at $T = [1, 2] \times 10^5$ K. We integrated this model with the effective area of the *GALEX* FUV detector (see Figure 1) and found that the CIV emission is $[40\%, 80\%]$ of the emission integrated over the FUV band. Taking the average we find the line emission from the HIM contributes $1.875 \times 4600 = 8625$ LU to the FUV band. The effective width of the *GALEX* FUV band is 255 Å (Table 3). Thus, the HIM contribution to the FUV background is 34 CU.

4.3. *Low-velocity Shocks*

Shocks are a central topic in the study of the ISM. The post-shocked gas cools via line emission, free-bound and free-free emission. Libraries of spectra of cooling gas have been published with increasing sophistication; see Raymond (1979), Shull & McKee (1979) and Sutherland & Dopita (1993). Shocks, say those with velocities, $v_s \gtrsim 100\,\mathrm{km\,s^{-1}}$, are dominated by UV line emission and X-ray emission. In contrast, shocks with low-velocities, $v_s \lesssim 100\,\mathrm{km\,s^{-1}}$, cool H with decreasing contributions from C and Si as the plasma cools. The principal cooling lines of hydrogen include not only the resonance lines but also two-photon emission. In fact, one of the earliest and unambiguous detection of two-photon emission was from a Herbig-Haro object with a $100\,\mathrm{km\,s^{-1}}$ shock (Brugel et al. 1982; see also Dopita et al. 1982).

Two-photon emission was invoked in a recent investigation of the fascinating 30°-long Hα arc in Ursa Major (McCullough & Benjamin 2001; Bracco et al. 2020). Separately, Fesen et al. (2021), using *GALEX* FUV observations along with Hα and radio imaging, uncovered three very large supernova remnants. In both cases, the underlying cause of two-photon emission is low-velocity shocks, $v \lesssim 100\,\mathrm{km\,s^{-1}}$.

These two results led us to investigate the entire class of low-velocity shocks as a major class of two-photon emission. The galaxy abounds in low-velocity shocks. All high velocity shocks eventually cascade to low-velocity shocks. In fact, the classical explanation for the observed $\approx 10\,\mathrm{km\,s^{-1}}$ velocity dispersion of the CNM is the stirring of the ISM by supernovae (§12.2c, Spitzer 1978; Kim & Ostriker 2015).

We draw attention of the reader to an observational support for this "shock→stir cascade" model – a study of the integrated H I spectrum towards the Galactic poles (Kulkarni & Fich 1985). These authors found a rather curious result: $N_H(v)v^2$ is flat out to $80\,\mathrm{km\,s^{-1}}$; here, v is the velocity and $N_H(v)$ is the column density of H atoms with velocity v. Separately, the H I spectrum towards the South Galactic pole shows no mean motion whereas strong inflow can be inferred from the spectrum towards the North Galactic pole. We first consider the zero velocity component and postpone the discussion of in-falling (negative velocity) gas. We interpret the velocity width of this component as arising from thermal and turbulent motions of the H I gas that has recombined and is cooling. In the cascade model, $N_H(v)v^2$ can be interpreted as a product of the particle flux, $N_H(v)v$, and the momentum per particle ($\propto v$). Thus, the Galactic pole H I observations inform us that the momentum flux is constant. This inference is in accord with our expectation that already by $80\,\mathrm{km\,s^{-1}}$ shocks are "momentum conserving" (aka "snowplow" phase of SNRs). In contrast, the energy flux $\propto N_H(v)v^3 \propto v$. Thus, radiative shocks are losing energy proportional to their velocity. This is perhaps a simplistic analysis in that we have not tracked the ionization state of cooling hydrogen. Nonetheless, this analysis prepares us to accept a low efficiency for stirring.

The mass of the Galactic H I gas is $M_{\rm HI} = 3 \times 10^9\,M_\odot$ (Chapter 1 of Draine 2011). The Galactic supernova (SN) rate is conservatively estimated to be one per century or $\dot{E}_{\rm SN} = 3 \times 10^{41}\,\mathrm{erg\,s^{-1}}$, assuming 10^{51} erg per SN. Let η be the conversion efficiency of SN energy that goes into the stirring of the atomic phases and let σ_{HI} be the effective rms velocity of CNM+WNM. Then the mean time between successive stirrings is

$$\tau_{\rm HI} = \frac{1/2 M_{\rm HI}\sigma_{HI}^2}{\eta \dot{E}_{\rm SN}} \approx 10^{13}\eta^{-1}\sigma_6^2\,\mathrm{s}, \qquad (1)$$

where $\sigma_{HI} = 1 \times 10^6 \sigma_6\,\mathrm{cm\,s^{-1}}$. Locally, the vertical column density towards the Galactic poles is $N_H \approx 2 \times 10^{20}\,\mathrm{atom\,cm^{-2}}$ (Lockman & Gehman 1991). Thus, the rate of successive SN impacts in a vertical column is

$$\mathcal{F}_{\rm SN} = N_H/\tau_{\rm HI} = 2 \times 10^7 \eta \sigma_6^{-2}\,\mathrm{atom\,cm^{-2}\,s^{-1}}. \qquad (2)$$

In order to convert $\mathcal{F}_{\rm SN}$ to two-photon decays we make the following (conservative) assumptions: (1) we restrict to shocks with initial velocity, $v \gtrsim 100\,\mathrm{km\,s^{-1}}$. Such shocks will pre-ionize the ambient gas (Raymond 1979; Shull & McKee 1979). (2) In the post-shocked region each H ion undergoes only one recombination, (2) a third

of case B recombinations lead to two-photon emissions and (3) following recombination, no H atom is collisionally excited to the 2s state or 3p state. With these assumptions, the columnar rate of two-photon decay is $\mathcal{R} = {}^1\!/_3\mathcal{F}_{\rm SN}$.

McKee & Ostriker (1977), in the framework of the 3-phase model for the ISM, found $\eta = 0.05$. Kim & Ostriker (2015) carry out a detailed simulation and find that each SN (with $E_0 = 10^{51}$ erg of explosive energy) has, at the onset of the formation of radiative shells ("snowplow" phase), a momentum of $p_{\rm sf} = 2\times10^5 n_0^{-0.15}\,M_\odot{\rm km\,s^{-1}}$ where n_0 is the particle density of the medium into which the SN exploded. If we assume that all this momentum results in stirring of clouds (velocity dispersion, σ) then $\eta = 1/2(p_{\rm sf}/\sigma)\sigma^2/E_0 \approx 2\sigma_6\%$. I note that in the Kim & Ostriker (2015) model, the expansion velocity at the time of shell expansion is $v_{\rm sf} = 200\,{\rm km\,s^{-1}}$. If we accept the inference discussed above (cf., Kulkarni & Fich 1985) then $\eta = \sigma/v_{\rm sf} = 0.05\sigma_6$. So we elect to set $\eta = 0.05$ and then find $\mathcal{R} = {}^1\!/_3 \times 10^6\sigma_6^{-2}\,{\rm decay\,cm^{-2}\,s^{-1}}$. which corresponds to FUV brightness of 29 CU.

5. FLUORESCENCE OF LYβ PHOTONS

In the Solar system, in contrast to the WIM, the primary excitation of H atoms is not by photo-ionization but due to excitation by solar Lyman series photons (Lyα, Lyβ, Lyγ, etc.). There is a rich literature of both theory and observations related to diffuse Lyα in the Solar system.

In this paper we focus on Lyβ photons (λ_β = 1025.7220 Å). These photons excite H atoms to either $3{\rm p}\,^2P_{1/2}$ or $3{\rm p}\,^2P_{3/2}$ (a partial Grotrian diagram for H I is provided in Figure 3). The excited atom has two options: relax to the ground state by emitting a Lyβ photon (we denote the corresponding A-coefficient by A_{31}) or de-excite to the $2{\rm s}\,^2S_{1/2}$ state by emitting an Hα photon (A_{32}). The branching ratio to emit Lyβ is $B = A_{31}/(A_{31}+A_{32}) = 0.88$. We let $\eta_{H\alpha} \equiv A_{32}/A_{31} \approx 1/7.4$. For higher order Lyman series photons the probability to reach the $2{\rm s}\,^2S_{1/2}$ level is smaller. Furthermore, an inspection of the solar spectrum shows that the intensity of the higher lines is smaller than that of the Lyβ line. As a result, we simplify by restricting our analysis to only Lyβ excitations.

Our goal in this section is to compute the rate of excitation of H atoms by Lyβ photons. For this exercise we need to understand the frequency (velocity) profile of both solar Lyβ and that of H atoms. The geo-coronal H atoms, with respect to the Sun, have essentially zero radial velocity and a thermal velocity full-width at half-maximum (FWHM) of $7\,{\rm km\,s^{-1}}$. The H atoms in the IPM have a mean velocity of $-24\,{\rm km\,s^{-1}}$ with respect to the Sun. The thermal velocity spread of those H atoms is $18\,{\rm km\,s^{-1}}$.

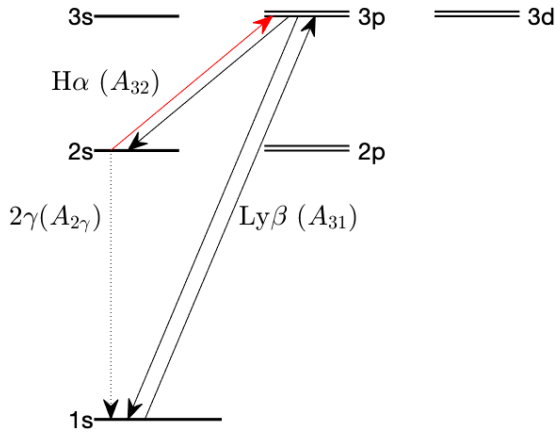

Figure 3. Partial Grotrian diagram for H I (not to scale). An H atom excited by Lyβ to 3p state has two choices: de-excite to ground state by emitting Lyβ (probability of $\approx 7/8$) or de-excite to the $2{\rm s}\ ^2S_{1/2}$ level by emitting Hα. For the latter case, in the absence of collisions, over a timescale of $A_{2\gamma}^{-1} \approx 0.12$ s, the atom de-excites by emitting two-photons. During this period, it can be excited by solar photons: bound-bound process such as Hα (shown) and bound-free process (see §B for discussion).

The solar Lyβ line has a velocity profile with two horns separated by about 0.33 Å and a full-width-at-zero of 1 Å (Figure 4). In other words, the velocity width of Lyβ is quite narrow, $\pm50\,{\rm km\,s^{-1}}$. It requires a very high resolution spectrometer to see the structure of this line. Fortunately, a linear relation exists between the intensity at the valley center and the integrated Lyβ emission. This relation allows solar astronomers to infer the zero velocity (central) Lyβ intensity from integrated Lyβ observations.

Over the period 1996–2009 (solar cycle 23), the central photon flux density at 1 AU varied from $4\times10^{10}\,{\rm phot\,cm^{-2}\,s^{-1}\,nm^{-1}}$ to $10\times10^{10}\,{\rm phot\,cm^{-2}\,s^{-1}\,nm^{-1}}$ (Lemaire et al. 2015). We adopt the minimum flux for our fiducial value. We also switch to the non-CGS but traditional Å unit but only for the differential wavelength (and not all other length quantities!) and thus $F_\lambda(\beta, v=0) = 4\times10^9\,{\rm phot\,cm^{-2}\,s^{-1}\,Å^{-1}}$. Here, v is the radial velocity between the absorbing H atoms and the mean velocity of the Sun. As a result of this curious but traditional choice of using Å for differential wavelength, $\nu F_\nu = (10^8 F_\lambda)\lambda$ and thus

$$F_\nu(\beta, v=0) = 1.4\times10^{-3}\,{\rm phot\,cm^{-2}\,s^{-1}\,Hz^{-1}}. \quad (3)$$

Going forward, we use the short hand $F_\nu(\beta, v=0) = F_\nu(0)$ and so on.

The frequency-dependent absorption cross-section is

$$\sigma_{lu}(\nu) = \frac{\pi e^2}{m_e c} f_{lu} \phi_\nu \tag{4}$$

where l (u) stands for lower (upper) levels and ϕ_ν is the probability distribution as a function of frequency for the absorption process, $\int \phi_\nu d\nu = 1$. The oscillator strength, f_{lu}, is related to the A-coefficient as follows:

$$A_{ul} = \frac{8\pi^2 e^2 \nu_{ul}^2}{m_e c^3} \frac{g_l}{g_u} f_{lu} = \frac{0.6670}{\lambda_{lu}^2} \frac{g_l}{g_u} f_{lu} \,\mathrm{cm^2\,s^{-1}}. \tag{5}$$

This probability density function is the convolution of the natural broadening function (Lorentzian with a frequency width of $A_{ul}/(2\pi)$) and a 1-D Gaussian distribution which accounts for Doppler-induced frequency shifts of moving atoms. The Lyβ column densities in the IPM and exosphere are, at best, mildly thick and so we can entirely ignore the "damping" or Lorentzian wings. If, as it happens to be the case, the photon intensity is constant over the spread in frequency due to thermal motions and that there is no relative radial velocity, v, between the absorbing photons and the Lyman series photons, then $F_\nu = F_\nu(v=0) = F_\nu(0)$ and the rate of excitation per atom is

$$\mathcal{R} = \int F_\nu \sigma_{lu}(\nu) d\nu = F_\nu(0) \frac{\pi e^2}{m_e c} f_{lu} \,\mathrm{atom^{-1}\,s^{-1}} \tag{6}$$

$$= 10^8 F_\lambda(0) \left(\frac{\lambda_{ul}}{\nu_{ul}}\right) \frac{\pi e^2}{m_e c} f_{lu} \,\mathrm{atom^{-1}\,s^{-1}}. \tag{7}$$

We first consider the simple case of a medium optically that is optically thin to Lyβ but has a low particle density (so that the probability of an H atom colliding with another particle, particularly a proton, over a duration of $A_{2\gamma}^{-1}$, is negligible). Let L_β (L_α) be the *photon* surface brightness of Lyβ (Lyα). The rate of Lyβ excitation per H atom is is obtained by evaluating Equation 7 with the flux given by Equation 3 is

$$R_\beta = 2.94 \times 10^{-6} d_{\rm AU}^{-2} \,\mathrm{atom^{-1}\,s^{-1}}. \tag{8}$$

The corresponding Lyβ surface brightness is $L_\beta = \mathcal{R}_\alpha N_H$ where N_H is the hydrogen column density, along the line of sight.

We now compute the ratio of the brightness of the scattered Lyα to that of Lyβ which is given by R_α/R_β. This ratio is the product of the ratio of luminosity of the solar Lyα to Lyβ and also the corresponding ratio of $\lambda^2 f_{lu}$ for the two lines. The ratio of the solar Lyα to Lyβ intensity (with intensity expressed in energy units and not photons) ranges from 50 (solar maximum) to 80 (solar minimum); see (Lemaire et al. 2012). Thus the ratio in photon flux of Lyβ to that of Lyα, hereafter $\eta_\odot$, ranges from 1/95 to 1/60. We adopt, the harmonic mean $\eta_\odot = 1/73$. The ratio of $\lambda^2 f_{lu}$ for the two lines is 7.4. Thus, for optically thin medium, $L_\beta \approx L_\alpha/540$. The surface brightness in Hα, $L_{H\alpha} = \eta_{H\alpha} L_\beta \approx L_\alpha/4000$.

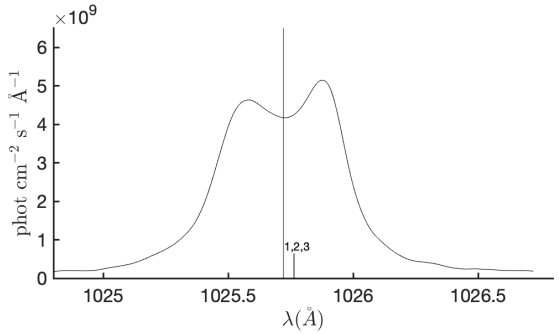

Figure 4. The profile of solar Lyβ. The continuum level in the vicinity of this line is very small, 6×10^7 phot cm^{-2} s^{-1} Å^{-1} (see Figure 2 of Dudok de Wit et al. 2005 for an annotated EUV/FUV solar spectrum). The vertical line marks the rest wavelength of Lyβ. Three resonance lines of O I (marked as "1,2,3", corresponding to lines with internal index 1, 2, 3 in Table 5), represented by vertical stubs but are so close to each other that the stubs overlap fully. The remaining three O I lines (index 4, 5, 6) lie outside the displayed spectral window; see §E for further details. The Lyβ spectral data is from the SOHO mission (Lemaire et al. 2015).

There is an important and interesting complication for H atoms in the inner solar system. Recall that an H atom which absorbs a Lyβ photon emits Hα with a probability of $1 - B$ (see §5) and reaches the 2s level. If undisturbed over a period of $A_{2\gamma}^{-1}$ the atom decays to ground state by emitting two-photon continuum. However, during this waiting period, solar photons can excite the H atom to a higher level by absorbing, for example, an solar Hα photon or ionize the H atom by absorbing a blue/UV photon. In §B we show that the process results in an a pumping rate, $A_p \approx 2.2 d_{\rm AU}^{-2}\,\mathrm{s^{-1}}$ where $d_{\rm AU}$ is the distance of the hydrogen atom from the Sun in units of AU. Thus, solar optical pumping reduce the two-photon emission probability by $p_{2\gamma} = A_{2\gamma}/(A_{2\gamma} + A_p)$. Upon absorption of Ly$\beta$, the branching ratio for two-photon production is $(1-B)p_{2\gamma}$ while that for Lyβ scattering is $1 - (1-B)p_{2\gamma}$. In contrast, the probability of Hα emission, upon absorption of Lyβ, is independent of solar pumping. Note that for $p_{2\gamma} \ll 1$ Lyβ photons are not destroyed by fluorescence. Next, if the medium is optically thick to Lyβ and if optical pumping is not significant then most of Lyβ photons will be converted to Hα, two-photon continuum and Lyα Equally, if solar optical pumping is strong then the result is Hα and Lyβ.

We are now in a position to estimate the two-photon contribution from the Solar system: the interplanetary

medium (§6), the thermosphere of Earth (§7) and the exosphere of Earth (§8). We end this section by discussing two-photon emission from other objects in the solar system. Ground-based Fabry-Perot telescopes readily detect atomic hydrogen from comets (Shih et al. 1984). This bodes well for detection of two-photon emission from comets. Next, since $A_p \propto d_{\rm AU}^{-2}$, solar photon pumping will reduce two-photon emission of objects in the inner solar system. However, Hα production is not affected.

6. INTERPLANETARY MEDIUM

The entire Solar system is moving into a local interstellar cloud at a velocity of about 25 $\rm km\,s^{-1}$. From high-resolution spectroscopic UV studies the following properties of the interstellar cloud have been deduced: neutral H density of 0.1 $\rm cm^{-3}$, temperature of 7000 K and 50% ionization fraction (Frisch et al. 2011; Gry & Jenkins 2017). These properties seem to have physical attributes similar to the WNM, albeit with a high fractional ionization and also a low column density. While astronomers refer to this cloud as the "very local ISM" (VLISM) planetary astronomers call this medium as the interplanetary medium (IPM).

The Sun has a weak wind, about $10^{-14}\,M_\odot\,\rm yr^{-1}$. The wind is correlated with solar activity and also has dependence on solar latitude and longitude (Prölss & Bird 2004). At 1 AU, the typical properties are as follows: electron density, n_e of 3–10 $\rm cm^{-3}$, magnetic field strength of 10–370 μG and temperature of 10^5 K. By the time the wind reaches Earth it is supersonic, $v_{\rm wind} \approx 500\,\rm km\,s^{-1}$. For a spherical and steady wind, conservation of mass leads to a decrease in density as r^{-2}. The solar wind is neither steady nor spherically symmetric. However, averaged over a solar cycle, $n_e \propto r^{-2}$ where r is the heliocentric radius.

The fast solar wind comes to equilibrium with the slow moving interstellar medium by undergoing a shock – the so-called solar wind termination shock (SWTS). In the parlance of planetary astronomers, the surface separating the shocked solar wind and the interstellar gas is called the heliopause (aka "contact discontinuity" for astronomers). Thanks to the Voyager missions we know that the SWTS is located at 90 AU while the heliopause is at 120 AU.

The neutral particles of the VLISM/IPM are not affected by the shock fronts. H atoms scatter solar Lyα and create a haze on the sky. The present picture of an incoming interstellar wind was initially deduced by detection of the Lyα haze by OGO-5 (Bertaux & Blamont 1971; Thomas & Krassa 1971). As it so happens, for H atoms, the radiative repulsion is almost canceled by the gravitational acceleration (see see Kurt et al. 2009 for a review). In contrast, for He atoms the radiative pressure is small and so they are gravitationally focused by the time they arrive in the the inner Solar system. The direction of the wind was deduced from the distribution of the Lyα haze on the sky and refined by IBEX using *in situ* measurements of He I (Frisch et al. 2013). Gry & Jenkins (2017) provide a nice review of the velocity vector of the solar system relative to the local interstellar cloud.

The "downwind" direction of the wind in ecliptic longitude (λ) and latitude (β) coordinates is 79° and −5° which corresponds to Galactic coordinates $l = 185°$ and $b = -12°$ (Frisch et al. 2013). The upwind direction, $l = 5°$ and $b = 12°$, corresponds to a direction just "above" Scorpius constellation but "below" Ophiuchus.

The rate of photo-ionization by the solar Lyman continuum is $\mathcal{R}_{\rm pi} = 6 \times 10^{-8} d_{\rm AU}^{-2}\,\rm s^{-1}$ where $d_{\rm AU}$ is the heliocentric distance in AU. The rate of charge exchange, assuming mean solar wind properties, is $\mathcal{R}_{\rm ce} = 6 \times 10^{-7} d_{\rm AU}^{-2}\,\rm s^{-1}$. Upon charge exchange, the newly minted H^+ is subject to electrical and magnetic forces of the solar wind and acquires the velocity of the solar wind. The resulting large velocity places the atom outside the narrow solar Lyβ line.[6] and so these atoms can no longer serve as sources for two-photon production. The recombination timescale for a newly ionized H^+ particle is considerably longer than the crossing time across the Solar system. So the ionized cavity is highly anisotropic with strong Lyα haze in the upwind direction and a considerably weaker haze in the downwind direction. The Lyα production peaks in the heliocentric annulus 2–5 AU in the upwind direction.

6.1. *Measurements*

Voyager-2 was launched on 1977 August 20. One month later, when the spacecraft was at a heliocentric distance[7] of 1.02 AU, the UV spectrometer was pointed to $\alpha = 324°$ and $\delta = -23°$. It detected Lyα at $722 \pm 0.5\,R$, Lyβ at $2 \pm 0.16\,R$ and Helium 584 Å at $3.8 \pm 0.04\,R$ (Sandel et al. 1978). Next, long observations of several high Galactic latitude fields were undertaken in February and March, 1981 (heliocentric distance of 8.4 AU). These observations detected not only Lyβ but also higher order Lyman lines (Holberg 1986). Of interest to us were $L_\alpha = 1080\,R$ and $L_\beta = 2.4\,R$. The

[6] The width of the Solar Lyα line as measured from horn-to-horn and width-at-half maximum is $\pm 75\,\rm km\,s^{-1}$ and $\pm 125\,\rm km\,s^{-1}$, respectively.

[7] The distance to Voyager-2 was computed using a tool provided at https://omniweb.gsfc.nasa.gov/coho/helios/heli.html

ratio between Lyα and Lyβ seems to be consistent with that expected for optically thin medium (§5). The New Horizons mission also carried a UV spectrometer and detected Lyα surface brightness of 550 R at a heliocentric distance of 7.6 AU decreasing to 100 R at 38 AU (Gladstone et al. 2018) – confirming that peak Lyα production takes place in the inner Solar system.

We now summarize this section. From our vantage point, in the "upwind" direction of the IPM, we see $L_\beta = 2.4\,R$. The expected two-photon decay rate is $\eta_{H\alpha} L_\beta = 0.33\,R$. The corresponding brightness in the FUV band is about 28 CU.

7. THE ATMOSPHERE OF EARTH

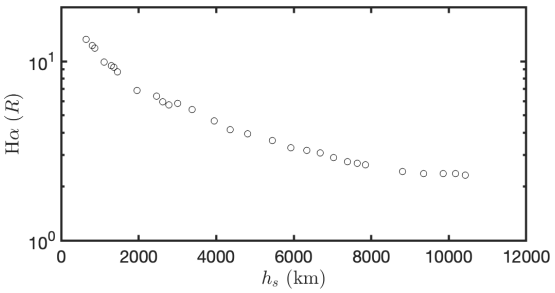

Figure 5. Representative zenith angle scan of geo-coronal Hα undertaken with WHAM at Kitt Peak National Observatory at dusk shown as a function of shadow height, h_s. The WHAM data are from Nossal et al. (2008) and obtained during February 2000 (solar maximum).

The same solar Lyman photons that excite the IPM also excite hydrogen atoms in the (upper) atmosphere and the exosphere. In fact, a by-product of Lyβ absorption is "geo-coronal" Hα which is routinely detected by the ground-based WHAM.

7.1. *Ground-based Hα Observations*

Typically, WHAM, during dusk and dawn, undertook scans as a function of zenith angle for aeronomical studies (see, for example, Nossal et al. 2008, 2019). It is traditional to report these scans (Figure 5) as a function of "shadow height" (see Figure 6 for definition and explanation). Note that within the shadow cylinder, in the absence of multiple scattering, no Hα emission will take place. However, Lyβ+OI and Lyα is clearly seen by LEO missions looking "upward" (and discussed in detail in §7.3). Detailed modeling (Bishop et al. 2001) show, in fact that, within the thermosphere (100-500 km) scattered Lyβ is comparable to the incident flux. Next, "cascade" or recombination from states higher than $n = 3$ contribute less than 10% of the Hα emission (Bishop et al. 2001). So, we will make the simplifying assumption that Hα is solely powered by Lyβ.

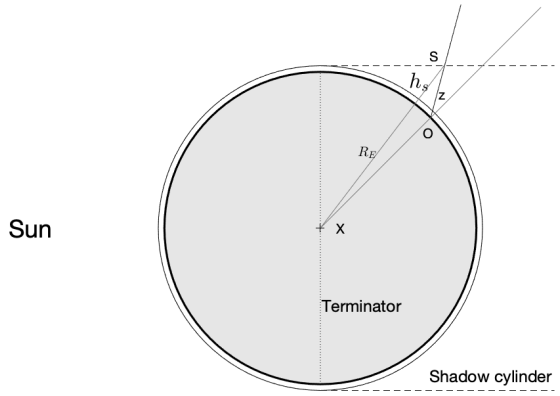

Figure 6. Illustration to explain the concept of shadow height or shadow altitude. The Earth is represented by a circle, radius R_E, with a thick black line perimeter. The lighter circle represents the typical height at which Lyβ is fully absorbed (about 100 km; primarily by molecular oxygen). The Sun is located to the left and casts a cylindrical shadow as illustrated by the dashed lines on the right side. The observer is located at "O" on the surface of Earth. The observer's line-of-sight, bearing zenith angle z, intersects the shadow cylinder at "S". The "shadow" height, h_s, is the radial distance above the Earth's surface to point S, h_s = XS − R_E where XS is the length of segment XS.

Typically the Hα surface brightness measured at zenith in the middle of the night[8] is 1.5 R at solar minimum and twice that at solar maximum (Nossal et al. 2008, 2019). Following the emission of an Hα photon the hydrogen atom finds itself in the 2s level. If the atom decayed by two-photon emission then the resulting two-photon brightness would be 85 CU per Rayleigh of Hα emission (§3) which, when summed with other sources of two-photon emission (§4, §6), would exceed the level of the offset emission of 120–180 CU (§2). This contradiction is attended to in the next discussion.

7.2. *Collisional Mixing of 2s and 2p states*

The energy difference between 2s and 2p is less than a milli eV. Recall that an atom excited to a 2s state decays to ground state on a timescale of $A_{2\gamma} \approx 0.12$ s. During this time collisions can perturb the atom so it switches to a 2p level which would then decay immediately (timescale, $A_{2p\to1s} \approx 10$ ns).

An H atom will undergo collision on a timescale of $(nq)^{-1}$ where $q = \langle\sigma v\rangle$, n is the density of the collider, σ is the cross-section for the interaction, v is the relative velocity between the collider and the excited H atom, and the angular brackets indicate averaging over a Maxwellian velocity distribution. The colliders can be

[8] in this case, the shadow height is essentially infinite since the the line-of-sight is anti-Sun.

neutral particles, protons and electrons. For the neutral particles we adopt a "hard sphere" model and set the cross-section to $\sigma = 10^{-16}\,\mathrm{cm}^2$. We compute the sum of the rates for collisions with all neutral species as a function of height. We find that the time scale for collisions is longer than $A_{2\gamma}^{-1}$ throughout the thermosphere (see right panel of Figure 13).

Normally, electrons are effective in collisional interaction with neutral particles. However, given the small energy difference between 2s and 2p levels, the slower moving protons are more effective than electrons in effecting these (primarily) angular-momentum changing 2s→2p transitions (Purcell 1952; see §B.1). A reasonable nighttime temperature for the thermosphere is $\approx 1,000\,\mathrm{K}$ (§F). Let q_{e+p} be the sum of the collisional coefficients for electrons and protons.[9] Matching the inverse mean time between collisions $n_p q_{e+p}$ to $A_{2\gamma}$ yields the critical density $n_{\rm crit} = A_{2\gamma}/q_{e+p} \approx 10^4\,\mathrm{cm}^{-3}$ where n_p is the mean proton density. The production of two-photons becomes inefficient by $(1+n_p/n_{\rm crit})$. From Figure 14 we see that the proton density is below this critical density for heights above 1,200 km. In summary, two-photon emission is suppressed below 1,200 km due to collisional mixing of the 2s-2p states.

Table 1. STP 78-1 EUV observations of night glow

Line	"Up" (R)	"Down" (R)
Lyβ, OI	8.76 ± 0.3	2.3 ± 0.23
Lyα	3533 ± 5.8	1712 ± 4.7
OI 1304	7.1 ± 0.4	53.8 ± 1.3
OI 1356	< 2	52.2 ± 0.8

7.3. *Observations by Low-Earth Missions*

In this section, we review observations of Lyβ from space missions and conclude with an analysis.

7.3.1. *Measurements*

The Space Test Program 78-1 (STP 78-1; aka "Solwind")[10] was launched in 1979 into a sun-synchronous orbit (600 km height). The satellite spin-orbital axis was perpendicular to the Earth-Sun axis (i.e., a "noon-midnight" orbit). It carried, amongst other instruments, an EUV/FUV spectrometer for studies of airglow (Chakrabarti et al. 1984). The spectrometer had an entrance window of $18° \times 9°$ and operated over 350–1400 Å band. Chakrabarti et al. (1984) reported satellite nighttime EUV spectrum of airglow, both looking "down" (zenith angle, z, between 120° and 150°) and looking "up" (zenith angle between $30° < z < 80°$); here, zenith angle of 0° corresponds to the anti-sun direction. The relevant measurements are summarized in Table 1.

The Spanish Minisat-01 spacecraft (Morales et al. 1998) carried a high spectral resolution EUV spectrometer, EURD ("Espectrógrafo Ultravioleta extremo para la Radiación Difusa"; Edelstein et al. 2006). The orbit was a circle with height of 580 km and inclined 151° with respect to the equator. Observations were obtained only during satellite midnight, specifically restricted to zenith angle of −85° (just before ground dawn)[11] and +80° (just after dusk). Restricting to absolute zenith angle of $< 70°$, Lyβ was detected at a level of $6.4\,R$ (López-Moreno et al. 2001).

7.3.2. *Bowen Fluorescence of O I and Lyβ*

The STP 78-1 and EURD measurements are listed as Lyβ+OI because there happens to be a near coincidence between the wavelength of Lyβ and some resonance lines of O I (see §E and Figure 16). The transition is composed of six lines of which three (hereafter, the "trio") lie only about $+8\,\mathrm{km\,s}^{-1}$ of the rest wavelength of Lyβ and the other three are several hundreds of $\mathrm{km\,s}^{-1}$ away. The trio, thus, are readily excited by solar Lyβ photons (but the other three are not). Each such excitation results in re-emission of the incident photon (71%) which will be indistinguishable from Lyβ or fluorescence via emission of the O I 1304 Å triplet (see Figure 16). Next, the sum of the oscillator strengths for the trio is $f_{\rm trio} = 0.0201$ which can be compared with $f_\beta = 0.0791$, the oscillator strength for Lyβ. However, do note that the atomic oxygen density in the thermosphere exceeds that of atomic hydrogen.

7.3.3. *Analysis*

We consider the upward Lyβ+OI emission. The observed Lyβ+OI brightness sets an upper limit to the surface brightness of Lyβ. The brightness of λ1304 Å (which can also be directly excited by solar OI photons) means that a good fraction of the observed Lyβ+OI must be due to scattering by O I. On the other hand, for optically thin conditions, the ratio of Lyα to Lyβ is 400 which should be compared with 540 (§5). Assuming optically conditions for all lines (Lyα, Lyβ and OI) lead

[9] Ions such as O^+ are even more effective because of their slower velocities. However, by 1,000 km heigh the dominant species is H and not O; see Figure 13.

[10] Unfortunately, towards the end of the mission, Solwind was assigned as target for a pilot demonstration of anti-satellite technology (ASAT). On September 13, 1985 the satellite was destroyed by an ASM-135 missile mounted on an F-15 fighter airplane.

[11] the authors appear to have assigned a sign to z depending on whether line-of-sight is towards East or West

us to conclude that about 3/4 of the upward brightness is due to Lyβ.

The downward Lyβ+OI surface brightness is 2.3 R. This should be contrasted with the (upward) ground-based geo-coronal emission of 1.5 R (solar minimum) or 3 R (solar maximum). The only way to reconcile these two measurements is to ascribe most of the ground-based (integrated) Hα emission to an altitude above the orbital height of Solwind. However, Bishop et al. (2001) argue that bulk of this Hα arises from atomic hydrogen between 100 and 500 km. Their model hydrogen column density over this range of height of 6×10^{13} cm^{-2} is five times larger than that provided by the standard MSIS (Mass Spectrometer and Incoherent Scatter radar) model (see Figure 13). This is a rather surprising conclusion given that, in the standard MSIS model, O I dominates over H I for heights below 800 km (Figure 13; see §C for further discussion).

Overall, the situation is unsatisfactory. Lyα is optically thick whereas Lyβ is mildly optically thick and is confused by Bowen fluorescence with O I. Hα is not optically thick but the primary measurement is integrated Hα (from ground-based facilities). A consistent full-blown radiative transfer modeling of both oxygen and hydrogen lines is needed to infer the vertical distribution of oxygen and hydrogen. A more robust approach would be to space-based measurements in Hα (§10).

Parenthetically, we note that Ake (2012), from an analysis of HST FUV spectroscopic data, report night time Lyα surface brightness of 2 kR. The difference between this value and the one given in Table 1 is likely due to the aeronomy measurements being done at relatively high zenith angles, $z > 30°$.

8. THE EXOSPHERE

The exobase is the bottom of exosphere (and the top of the thermosphere; see §C). At the high temperature of the exobase, H and He achieve sufficient velocity to escape from Earth (§F). As can be seen from Figure 7 the exosphere appears to extend to a distance well beyond that of the orbit of the moon.

As can be seen from Figure 8 the hydrogen column densities above 1,000 km is approximately 10^{13} cm^{-2}. The corresponding central optical depth in Lyman-β is given by

$$\tau_0 = 0.32\Big(\frac{N_l}{10^{14}\,\mathrm{cm}^{-2}}\Big)\Big(\frac{5\,\mathrm{km\,s}^{-1}}{b}\Big) \qquad (9)$$

where $b = \sqrt{2}\sigma_v$ and σ_v is the Gaussian velocity width. Thus, τ_0 is less than unity and so the two-photon brightness is $\eta_{H\alpha} L_\beta$.

8.1. *Lyβ scattering during night time*

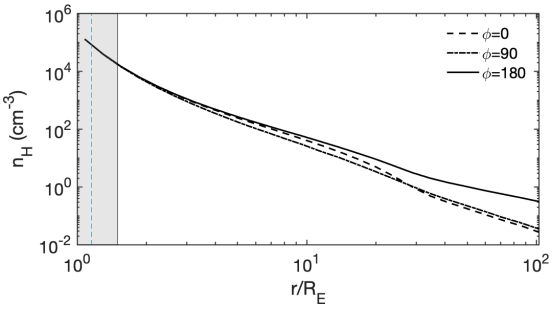

Figure 7. Top: The density profile of H atoms as derived from *SWAN-SOHO* measurements (Baliukin et al. 2019). Here, R_E is the radius of Earth. The dashed vertical line marks height of 1,000 km. Owing to the angular resolution of *SWAN* the model is not reliable for radius less than 1.5 R_E (shaded region). ϕ is the angle between line-of-sight and the Sun. Thus the night-time radial profile is described by $\phi = 180°$ model whereas $\phi = 0°$ applies to the model at noon time. Note the exosphere has a larger radial extent on the night side, compared to the day side ("geotail"). On a timescale of about six months H atoms which escape Earth are ionized by the solar Lyman continuum (see §6). The model data were supplied by I. Baliukin.

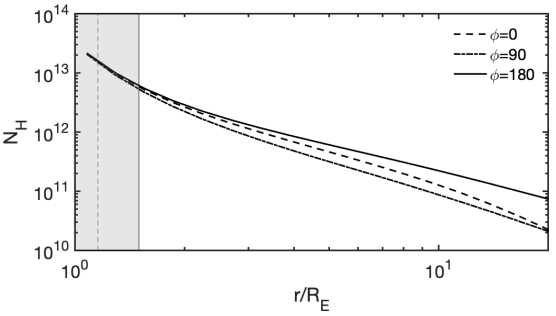

Figure 8. The column density of H I atoms obtained by integrating the density displayed in Figure 7.

We now compute Lyβ scattering during Earth eclipse as observed by a satellite in a circular orbit of height h, at local midnight. To this end, we integrate the H atom density along a line-of-sight bearing a constant zenith angle, z, for such a satellite on the night side. The exosphere density is decreasing reasonably rapidly with radius. So, not much error is made in replacing the conical umbra with a cylindrical shadow. From vector algebra and trigonometry we find

$$r^2 = r_s^2 + l^2 + 2 r_s l \cos(z), \quad \sin(\phi) = \frac{d}{r}\sin(z), \qquad (10)$$

where $r_s = R_E + h$ is orbital radius of a satellite at height h and l is the distance measured from the satellite along a given line-of-sight (see Figure 9 for geometry). The resulting Lyβ photon surface brightness is $L_\beta = (1/4\pi) N_H \mathcal{R}_\beta$ where $N_H = \int n_H(r) dl$, the column density along the line-of-sight, and the per atom rate of

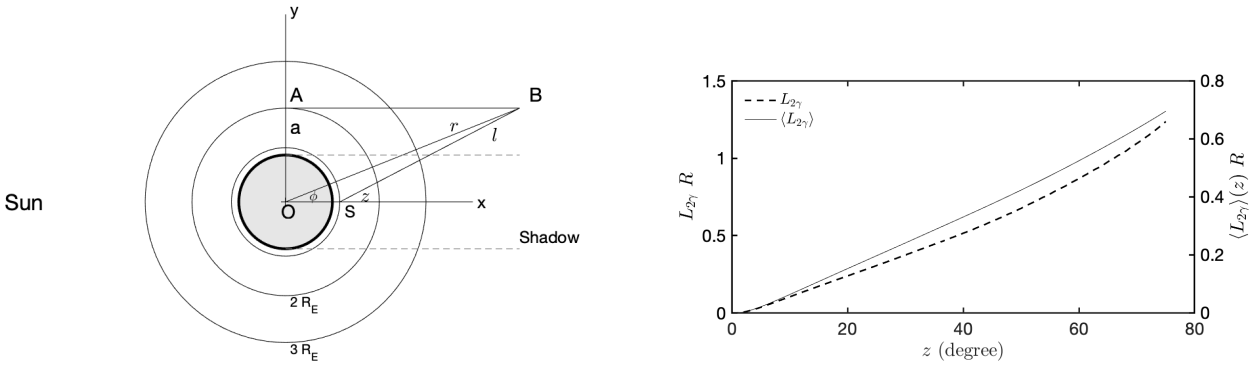

Figure 9. (*Left*): Geometry of the Exosphere. The Cartesian coordinate system is centered at the Earth's center with x towards the Sun and y towards the terrestrial North pole. For simplicity we assume that the Earth's rotation axis is perpendicular to the Sun-Earth line. The inner-most dark circle with radius R_E represents Earth. The radius of the next circle is $r_s = R_E + h$ and the circle represents the orbit of a satellite at height h (marked "S"). The next two circles have radii of $2R_E$ and $3R_E$. The impact parameter, a, is the segment OA. The umbra cast by Earth is a cone with a depth of $215\,R_E$. We simplify by replacing the umbra-penumbra combination with a cylinder (dashed lines; "Shadow"). Consider a line-of-sight originating from the aforementioned satellite going towards point B (which is at radius r). Let z be the zenith angle, measured from x axis in a counter-clockwise fashion, and ϕ the corresponding geo-centric polar angle. l (OB) is the distance measured from the satellite to point B whereas r is geo-centric distance to point B. (*Right*): The model two-photon surface brightness in Rayleigh expected at night time as a function of the fraction of the sky, as measured along angle z of the satellite.

excitation, $\mathcal{R}_\beta$, is given by Equation 8. The corresponding two-photon emission per atom rate is $(1 - Bp_{2\gamma})R_\beta$.

For $h = 1,000$ km in Figure 9 we display $L_{2\gamma}$ as a function of the satellite zenith angle. We see that in our simple single-scattering model there is no two-photon emission at zenith. However, there is evidence of Lyβ photons in the shadow cylinder. First, the upward looking Lyβ+OI (§7.3) is substantial, $\approx 8\,R$. Next, O I $\lambda\,1304$ Å triplet is seen by HST at local midnight. This bright line is a result of Bowen fluorescence of O I powered by Lyβ photons (§C). Clearly, Lyβ must be scattered into the shadow cylinder.

We make the simplistic assumption that the scattered photons "fill up the trough" in Figure 9. We adopt the value at $z = 45°$ (which defines the edge of the shadow region for *GALEX*) observations which then results in $0.4\,R$ (when integrated over the FUV band) in two-photon continuum. The corresponding two-photon contribution is 34 CU.

9. SUMMING UP

We started the paper by noting that at high latitude 120–180 CU of the *GALEX* FUV could not be accounted by EBL and DGL (§2). In successive sections (§4-8) we undertook a systematic examination of two-photon emission from the WIM, low-velocity shocks, and the Solar system as well as line emission from the HIM. The resulting estimates are summarized in Table 2 above. We find that 110–148 CU of the *GALEX* FUV background can be attributed to these sources.

We now address the uncertainties of the entries in Table 2. In my view, the contributions from the WIM, the HIM and IPM rest on reliable measurements and robust theory (WIM: classical theory of recombination; HIM: direct observations; IPM: basic physics and robust measurements of solar EUV irradiance). The *mean* contribution from low-velocity shocks depends directly on the value of η which we have set to 0.05 (McKee & Ostriker 1977). If, on the other hand, it is 0.02 (Kim & Ostriker

Table 2. Inventory of diffuse FUV emission

Source	tracer	value	$\mathcal{B}$ (CU)
WIM	Hα	$0.4\,R$	23
HIM	C IV	8625 LU	34
Low-velocity shocks[a]	Hα	$0.34\,R$	12–29
IPM[b]	Lyβ	$2.4\,R$	7–28
Exosphere[b]	model	-	34
Total			110–148
Offset component	*GALEX*	-	120–180

NOTE—The source of emission is two-photon for all entries save the HIM (for which the source is line emission). [a]This entry is computed from a theoretical model. Restricted to shocks which are at least 100 km s^{-1}. Does not include contribution from collisional excitations nor contribution from local high velocity clouds .The fraction of SN energy which goes into cloud stirring is the principal uncertainty. [b]The intensity of IPM is brightest in the upwind direction and faintest in the opposite direction. Both IPM and Exosphere contribution scales directly with solar activity (EUV flux). Estimates presented here were computed for solar minimum.

2015) then the contribution from low-velocity shocks will be reduced to 16 CU. On the other hand, as explained in §4.3 the model used to compute the two-photon emission ignores collisional excitation and so undercounts the two-photon decays. A careful modeling of two-photon emission from radiatively cooling shocks (starting shock velocity of say, 100 km s^{-1}) would address this concern. A second and perhaps bigger concern is that while the two-photon emission from the mean infall is small it is possible that localized infall as seen towards the North Galactic pole (Kulkarni & Fich 1985) dominate.

In Table 2 we list the IPM contribution in the upwind direction. In the opposite direction, the two-photon contribution will be a quarter of this value or only 7 CU. Two-photon emission is certainly suppressed within the atmosphere and up to 1,200 km by 2s-2p collisional mixing. However, we lack reliable hydrogen density data between $h = 1,200$ km and $0.5\,R_E \approx 3200$ km. This contribution is not accounted for in Table 2.

9.1. *Temporal Variation*

The two-photon emission from the IPM as well as the exosphere scales directly with solar activity (solar EUV radiation). The solar EUV irradiance can, over a typical solar cycle, vary by factor of 2.5. In computing the contribution from the exosphere we adopted the solar minimum value for solar Lyβ irradiance (Equation 3). Thus, on statistical grounds the estimate given in Table 2 is assuredly an underestimate.

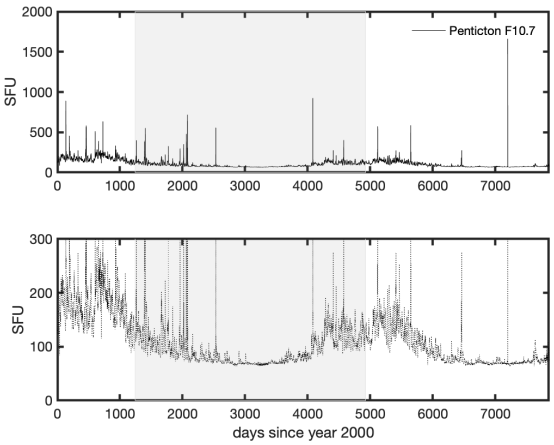

Figure 10. (Top) Light curve of solar 10.7-cm flux density (F10.7) since year 2000. (Bottom) Same data as top but with a smaller vertical scale. The shaded region is the period during which *GALEX* was operational. The short spikes are probably due to magnetic reconnection. The unit SFU stands for solar flux unit and is equal to 10^4 Jy. The measurements were obtained at the Dominion Radio Astrophysical Observatory, Penticton, British Columbia, Canada and the data were obtained from https://lasp.colorado.edu/lisird/.

A convenient surrogate for the EUV irradiance is provided by the 10.7 cm solar radio flux ("F10.7" index; see Tapping 2013). In Figure 10 we display this surrogate over the last two decades. The Sun appears to be quite variable not just on long timescales (solar cycle) but also much shorter timescales. We can expect that solar Lyman lines to be equally variable. Parenthetically, we note that evidence for variability in the FUV background can be readily seen in discordant "sky" values for adjacent pointings of GALEX FUV mosaic images (e.g., see Figure 2 of Fesen et al. 2021). In conclusion, it it appears that conventional possibilities can explain a good fraction of the FUV offset background.

9.2. *Diffuse NUV emission*

So far, we have focused on the FUV background. The NUV background, in addition to DGL and EBL, has an additional and dominant source: scattering of solar photons by zodiacal dust. Furthermore, it is bedeviled by a bright airglow line (O II $\lambda\lambda$ 2470.2, 2470.3 Å). These complications not withstanding, Akshaya et al. (2018) report "*an excess emission (over the DGL and the EBL) of 120–180 CU in the FUV and 300–400 CU in the NUV*". Applying the conversion factor given in Table 3 the two-photon excess in the NUV is modest, 20 CU or so. It would be useful to undertake a full calculation to see if processes which are expected to dominate in the NUV – free-bound and line emission from both WIM and HIM – are sufficient to explain the NUV offset emission.

10. CONCLUDING THOUGHTS

Diffuse FUV radiation plays a major role in the physics and chemistry of the Galactic diffuse interstellar medium. It provides primary inputs (heating, ionization, dissociation) to the diffuse atomic and molecular medium. As such, there has been considerable observational effort in measuring the FUV background. The diffuse FUV radiation seen at high Galactic latitudes has two components: FUV emission that is correlated with cirrus clouds and FUV that is independent of cirrus clouds. The former is simply stellar FUV light that is being reflected by dust particles. The latter consists of at least one component: collective emission from other galaxies (Extragalactic Background Light or EBL). Akshaya et al. (2019) estimate 60–81 CU from other galaxies, 16–30 CU from QSOs and < 20 CU from the IGM (and attributed to Martin et al. 1991). The total is 96-131 CU. After accounting for EBL we are left with some 120–180 CU of emission that has no obvious source counterpart and given the name "offset" component. This paper investigated FUV emission from the Galactic WIM and low-velocity shocks (two-photon emission),

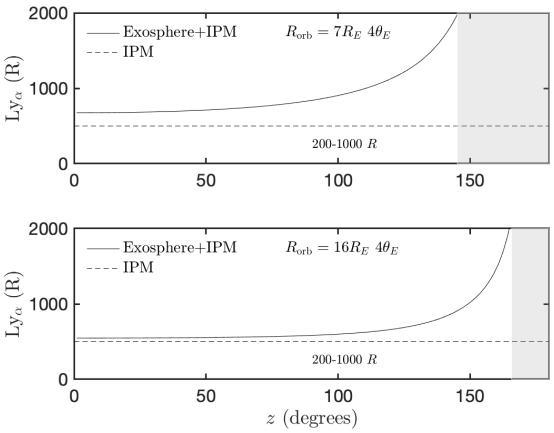

Figure 11. The expected Lyα background (in R) as a function of z for a satellite located in geo-synchronous orbit ($6.6\,R_E$; e.g., IUE or the planned Spektr-UF mission) and in High Earth Orbit (HEO; $16\,R_E$). The shaded region covers the zenith angle range of 180° to $180 - 4\theta_E$ where $\theta_E = \sin^{-1}(R_E/R)$ is the angular radius of Earth as seen from the vantage point of the satellite. The Lyα contribution from the IPM can range from 1,000 R to 200 R (see §6). In this figure, the IPM contribution is fixed to 500 R.

HIM (line emission) and two-photon emission from three locales in the Solar system: the interplanetary medium, the thermosphere and the exosphere of the Earth. As summarized by Table 2 It appears that these contributions collectively can account for two thirds or perhaps even all of the offset component.

Next, UV missions suffer less background by being in a high orbit (cf. IUE and the planned Spektr-UF/WSO mission). This is particularly important for FUV spectroscopic missions for which Lyα is both a key diagnostic and is also responsible for the background. In Figure 11 we compare the Lyα background for a mission in GEO and in HEO. Lyα background can be considerably reduced by undertaking observations at satellite zenith angle, $z \lesssim 90^\circ$ *and* preferentially studying regions of sky centered on the down-wind direction.

The discovery of three large SNRs (Fesen et al. 2021) was made possible, in part, by the distinctive FUV signature of low-velocity shocks. So, going forward, we have a new tool to identify low-velocity shocks – FUV and NUV imagery data. This is more sensitive than Hα searches because Hα from low-velocity shocks is broad in velocity and also has to compete with other sources (e.g., geo-corona, IPM and WIM).

We conclude with two proposals to further investigate the distribution of hydrogen in the thermosphere, the exosphere and the interplanetary medium. From the discussion in §7 it is clear that there is a tension between the amount of hydrogen in the thermosphere as deduced by modeling ground-based Hα data and the MSIS model. Furthermore, the modeling of LEO-based measurements of Lyβ+OI, complicated by Bowen fluorescence of O I, is not satisfactory. Space-based measurements of Hα brightness offer a clean way to model the vertical distribution of hydrogen. This can be accomplished with a cubesat equipped with narrow-band imagers and located in LEO .

Next, the ISM-Solar system interaction is a major area of research in space sciences. For a modest funding, relative to on-going and planned NASA investments, a ground-based facility with sensitivity ten times better than that of WHAM can be built. Such a facility can routinely detect surface brightness at the level of deci-Rayleigh. Solar EUV irradiance changes on a variety of timescales. It may be possible to measure the resulting Hα variations and thereby "plumb" the three-dimensional distribution of the IPM.

ACKNOWLEDGMENTS

What follows is an incomplete list of these who helped me. For help with ISM & Atomic Physics: Ronald Reynolds; Michael Shull, University of Colorado at Boulder; E. Sterl Phinney, California Institute of Technology. For help with FUV background: Jayant Murthy, Indian Institute of Astrophysics. For help with Aeronomy, SOHO and Voyager missions: Edwin J. Mierkiewicz & Matthew D. Zettergren, Embry-Riddle Aeronautical University; I. I. Baliukin, Space Research Institute (IKI), Moscow; and E. C. Stone, Project Scientist for Voyager Mission. For help with CHIANTI: Nikolaus Zen Prusinski, California Institute of Technology. For detector physics: Roger Smith, Caltech Optical Observatories. For feedback: Ilaria Caiazzo, California Institute of Technology; Bruce Draine, Princeton University; Jerry Edelstein & Christopher McKee, University of California at Berkeley; and Kevian Stassun, Vanderbilt University, Finally, I am most grateful to Robert Benjamin,University of Wisconsin at Madison; Hannah Earnshaw, California Institute of Technology; Eran Ofek, Weizmann, Institute of Science; and Michael Shull, University of Colorado at Boulder for careful reading and constructive feedback.

REFERENCES

Ake, T. B. 2012, in American Astronomical Society Meeting Abstracts, Vol. 219, American Astronomical Society Meeting Abstracts #219, 241.18

Akshaya, M. S., Murthy, J., Ravichandran, S., Henry, R. C., & Overduin, J. 2018, ApJ, 858, 101

—. 2019, MNRAS, 489, 1120
Baliukin, I. I., Bertaux, J. L., Quémerais, E., Izmodenov, V. V., & Schmidt, W. 2019, Journal of Geophysical Research (Space Physics), 124, 861
Barnes, K. L., van Zee, L., & Skillman, E. D. 2011, ApJ, 743, 137
Bertaux, J. L., & Blamont, J. E. 1971, A&A, 11, 200
Bertaux, J. L., Kyrölä, E., Quémerais, E., et al. 1995, SoPh, 162, 403
Bishop, J., Harlander, J., Nossal, S., & Roesler, F. L. 2001, Journal of Atmospheric and Solar-Terrestrial Physics, 63, 341
Bowen, D. V., Jenkins, E. B., Tripp, T. M., et al. 2008, ApJS, 176, 59
Boyarchuk, A. A., Shustov, B. M., Savanov, I. S., et al. 2016, Astronomy Reports, 60, 1
Bracco, A., Benjamin, R. A., Alves, M. I. R., et al. 2020, A&A, 636, L8
Brugel, E. W., Shull, J. M., & Seab, C. G. 1982, ApJL, 262, L35
Chakrabarti, S., Kimble, R., & Bowyer, S. 1984, J. Geophys. Res., 89, 5660
Chance, K., & Kurucz, R. L. 2010, JQSRT, 111, 1289
Cox, D. P. 2005, ARA&A, 43, 337
Deharveng, J. M., Joubert, M., & Barge, P. 1982, A&A, 109, 179
Del Zanna, G., Dere, K. P., Young, P. R., & Landi, E. 2021, ApJ, 909, 38
Dennison, B., Turner, B. E., & Minter, A. H. 2005, ApJ, 633, 309
Dere, K. P., Landi, E., Mason, H. E., Monsignori Fossi, B. C., & Young, P. R. 1997, A&AS, 125, 149
Dong, R., & Draine, B. T. 2011, ApJ, 727, 35
Dopita, M. A., Binette, L., & Schwartz, R. D. 1982, ApJ, 261, 183
Dove, J. B., & Shull, J. M. 1994, ApJ, 430, 222
Draine, B. T. 2011, Physics of the Interstellar and Intergalactic Medium (Princeton University Press)
Draine, B. T., & Bertoldi, F. 1996, ApJ, 468, 269
Drake, G. W., Victor, G. A., & Dalgarno, A. 1969, Physical Review, 180, 25
Dudok de Wit, T., Lilensten, J., Aboudarham, J., Amblard, P. O., & Kretzschmar, M. 2005, Annales Geophysicae, 23, 3055
Duley, W. W., & Williams, D. A. 1980, ApJL, 242, L179
Edelstein, J., Korpela, E. J., Adolfo, J., et al. 2006, ApJL, 644, L159
Fesen, R. A., Drechsler, M., Weil, K. E., et al. 2021, arXiv e-prints, arXiv:2102.12599
Frisch, P. C., Redfield, S., & Slavin, J. D. 2011, ARA&A, 49, 237
Frisch, P. C., Bzowski, M., Livadiotis, G., et al. 2013, Science, 341, 1080
Gladstone, G. R., Pryor, W. R., Stern, S. A., et al. 2018, Geophys. Res. Lett., 45, 8022
Gry, C., & Jenkins, E. B. 2017, A&A, 598, A31
Haffner, L. M., Reynolds, R. J., Tufte, S. L., et al. 2003, ApJS, 149, 405
Haffner, L. M., Dettmar, R. J., Beckman, J. E., et al. 2009, Reviews of Modern Physics, 81, 969
Haffner, L. M., Reynolds, R. J., Madsen, G. J., et al. 2010, in Astronomical Society of the Pacific Conference Series, Vol. 438, The Dynamic Interstellar Medium: A Celebration of the Canadian Galactic Plane Survey, ed. R. Kothes, T. L. Landecker, & A. G. Willis, 388
Hamden, E. T., Schiminovich, D., & Seibert, M. 2013, ApJ, 779, 180
Henry, R. C. 1991, ARA&A, 29, 89
Henry, R. C., Murthy, J., Overduin, J., & Tyler, J. 2015, ApJ, 798, 14
Holberg, J. B. 1986, ApJ, 311, 969
Jo, Y.-S., Seon, K.-I., Min, K.-W., Edelstein, J., & Han, W. 2017, ApJS, 231, 21
Jo, Y.-S., Seon, K.-i., Min, K.-W., et al. 2019, ApJS, 243, 9
Jura, M. 1974, ApJ, 191, 375
Kim, C.-G., & Ostriker, E. C. 2015, ApJ, 802, 99
Kollmeier, J. A., Weinberg, D. H., Oppenheimer, B. D., et al. 2014, ApJL, 789, L32
Kulkarni, S. R., & Fich, M. 1985, ApJ, 289, 792
Kurt, V. G., Mironova, E. N., & Fadeev, E. N. 2009, Cosmic Research, 47, 1
Kurt, V. G., & Sunyaev, R. A. 1970, in Ultraviolet Stellar Spectra and Related Ground-Based Observations, ed. R. Muller, L. Houziaux, & H. E. Butler, Vol. 36, 341
Lemaire, P., Vial, J. C., Curdt, W., Schühle, U., & Wilhelm, K. 2015, A&A, 581, A26
Lemaire, P., Vial, J. C., Curdt, W., Schühle, U., & Woods, T. N. 2012, A&A, 542, L25
Lockman, F. J., & Gehman, C. S. 1991, ApJ, 382, 182
López-Moreno, J. J., Morales, C., Gómez, J. F., et al. 2001, Ap&SS, 276, 211
Manchester, R. N., & Taylor, J. H. 1977, Pulsars (W. H. Freeman & Co)
Martin, C., Hurwitz, M., & Bowyer, S. 1990, ApJ, 354, 220
—. 1991, ApJ, 379, 549
Martin, D. C., Fanson, J., Schiminovich, D., et al. 2005, ApJL, 619, L1
McCullough, P. R., & Benjamin, R. A. 2001, AJ, 122, 1500
McKee, C. F., & Ostriker, J. P. 1977, ApJ, 218, 148

Meftah, M., Snow, M., Damé, L., et al. 2021, A&A, 645, A2
Meier, R. R., Anderson, D. E., J., Paxton, L. J., McCoy, R. P., & Chakrabarti, S. 1987, J. Geophys. Res., 92, 8767
Mende, S. B., Heetderks, H., Frey, H. U., et al. 2000, SSRv, 91, 287
Miller, Walter Warren, I., & Cox, D. P. 1993, ApJ, 417, 579
Morales, C., Gómez, J. F., Trapero, J., et al. 1998, Ap&SS, 263, 393
Morrissey, P., Conrow, T., Barlow, T. A., et al. 2007, ApJS, 173, 682
Murthy, J., Akshaya, M. S., & Ravichandran, S. 2019, arXiv e-prints, arXiv:1909.05325
Murthy, J., Henry, R. C., & Sujatha, N. V. 2010, ApJ, 724, 1389
Neufeld, D. A. 1990, ApJ, 350, 216
Nossal, S. M., Mierkiewicz, E. J., Roesler, F. L., et al. 2008, Journal of Geophysical Research (Space Physics), 113, A11307
—. 2019, Journal of Geophysical Research (Space Physics), 124, 10,674
Nussbaumer, H., & Schmutz, W. 1984, A&A, 138, 495
O'Connell, R. W. 1987, AJ, 94, 876
Osterbrock, D. E. 1974, Astrophysics of gaseous nebulae (W. H. Freeman and Company)
ØStgaard, N., Mende, S. B., Frey, H. U., Gladstone, G. R., & Lauche, H. 2003, Journal of Geophysical Research (Space Physics), 108, 1300
Paresce, F., & Jakobsen, P. 1980, Nature, 288, 119
Paresce, F., McKee, C. F., & Bowyer, S. 1980, ApJ, 240, 387
Prölss, G. W., & Bird, M. K. 2004, Physics of the Earth's Space Environment: an introduction (Springer)
Purcell, E. M. 1952, ApJ, 116, 457
Raymond, J. C. 1979, ApJS, 39, 1
Reynolds, R. J. 1990, ApJL, 349, L17
—. 1992, ApJL, 392, L35
Sandel, B. R., Shemansky, D. E., & Broadfoot, A. L. 1978, Nature, 274, 666
Savage, B. D., Sembach, K. R., Jenkins, E. B., et al. 2000, ApJL, 538, L27
Sciama, D. W. 1990, ApJ, 364, 549
Seon, K.-I., Song, H., & Chang, S.-J. 2021, arXiv e-prints, arXiv:2105.15062
Seon, K.-I., Edelstein, J., Korpela, E., et al. 2011, ApJS, 196, 15
Shih, P., Scherb, F., & Roesler, F. L. 1984, ApJ, 279, 453
Shull, J. M., & McKee, C. F. 1979, ApJ, 227, 131
Slavin, J. D., McKee, C. F., & Hollenbach, D. J. 2000, ApJ, 541, 218
Spitzer, Lyman, J., & Greenstein, J. L. 1951, ApJ, 114, 407
Spitzer, L. 1978, Physical processes in the interstellar medium (Wiley-Interscience), doi:10.1002/9783527617722
Stecker, F. W. 1980, PhRvL, 45, 1460
Sutherland, R. S., & Dopita, M. A. 1993, ApJS, 88, 253
Tapping, K. F. 2013, Space Weather, 11, 394
Thomas, G. E., & Krassa, R. F. 1971, A&A, 11, 218
Wild, J. P. 1952, ApJ, 115, 206
Witt, A. N., Gold, B., Barnes, Frank S., I., et al. 2010, ApJ, 724, 1551
Yao, J. M., Manchester, R. N., & Wang, N. 2017, ApJ, 835, 29
Zettergren, M. D., & Snively, J. B. 2015, Journal of Geophysical Research (Space Physics), 120, 8002

APPENDIX

A. TWO-PHOTON CONTINUUM

An H atom in the $2s\,^2S_{1/2}$ state radiatively decays by emitting two photons. The energies of the two photons add up to the energy of a Lyβ photon or 10.2 eV. The classical reference for the two-photon spectrum is Spitzer & Greenstein (1951) where they invoked the two-photon process to explain the continuum of planetary nebulae. The standard modern reference for the two-photon spectrum is Drake et al. (1969). Here, for the A-coefficient, we use the fitting formula of Nussbaumer & Schmutz (1984):

$$A(y) = CY[1-(4Y)^{\gamma}] + \alpha C Y^{\beta}(4Y)^{\gamma} \tag{A1}$$

where $y = \nu/\nu_0$, $Y = y/(1-y)$, $\nu_0 = c/\lambda_0$ and $\lambda_0 = 1215.67\,\text{Å}$ is the wavelength of Lyα. The fit values are $\alpha = 0.88$, $\beta = 1.53$, $\gamma = 0.8$ and $C = 202.0\,\text{s}^{-1}$. Since each de-excitation results in the emission of two photons, $\int_0^1 A(y)dy = 2A_{21} = 16.4\,\text{s}^{-1}$. Noting that $A(y)$ is the probability of emitting a photon in the frequency interval $dy = d\nu/\nu_0$ we find the emissivity from a single decay to be

$$j_\nu = \frac{1}{4\pi}\frac{h\nu}{\nu_0}A(y). \tag{A2}$$

Traditionally, observers use the spectral intensity as a function of wavelength, $j_\lambda = j_\nu \nu/\lambda$. The corresponding photon intensity is $n(\lambda) = j_\lambda/(hc/\lambda) \propto \nu j_\nu$. While $A(y)$ peaks at $y = 1/2$ corresponding to $\nu = \nu_0/2$ the spectral intensity j_λ peaks at 1400 Å (Figure 1).

Table 3. *GALEX* bands & response to two-photon decay

Parameter	unit	FUV	NUV
Bandpass	Å	1350–1750	1750–2800
FoV	deg^2	1.267	1.227
$\mathcal{I}$	cm^2Å	9402	45008
$\Delta\lambda_{\text{eq}}$	Å	255	730
$n(2\gamma)$	count	0.27	0.44
CR	$\text{phot}\,\text{s}^{-1}$	309	838
$\mathcal{B}_{2\gamma}$	CU	85.1	18.4

NOTE—The vital statistics of the FUV and NUV channels are summarized in the top half of the table. Here, $\mathcal{I} = \int A_{\text{eff}}(\lambda)d\lambda$ and $\Delta\lambda_{\text{eq}} \equiv \mathcal{I}/\max(A_{\text{eff}})$. $n(2\gamma)$ is the number of photons detected in each channel for a single two-photon decay. The last two lines are the response by the two *GALEX* channels to a uniform background from a column of 10^6 decays $\text{cm}^2\,\text{s}^{-1}$. CR is the counting rate across the entire detector for a two-photon while $\mathcal{B}_{2\gamma}$ is the inferred surface brightness (in CU).

The *GALEX* FUV band[12] is formally 1350–1750 Å while the NUV band is 1750–2800 Å (see Table 3). At one end of the probability distribution function (Equation A1), $y \to 1/2$, the two photons have equal energy in which case the

[12] The blue edge was chosen to avoid Lyα from Earth and the Interplanetary Medium as well as the bright airglow O I λ1304 Å triplet. These lines are bright: as seen by HST, Lyα is 2 kR (Ake 2012) while the O I line 13 R, even in Earth's deep shadow.

NUV band will register two photons. At the other end, $y \to 0$, one photon will get registered in the FUV band and the other will be in the optical/infra-red (OIR) band. Integrating over $A(y)$ we find that each decay results in 0.42 photons in the 1350–1750 Å band, 0.67 photons in the 1750–2800 Å band and 0.82 in the OIR band. [If the division is done by energy then the corresponding fractions are 33%, 37% and 30%].

However the *GALEX* passbands are not flat. Morrissey et al. (2007) provide a summary of the instrumental parameters[13] as a function of λ. For surface brightness, the FoV also matters. Morrissey et al. (2007) only provide a single FoV value, Ω, for each of the two channels. So we assume that, within each band, the FoV is independent of wavelength. For each channel, the band-pass weighted quantities for an input two-photon spectrum, is computed as follows,

$$j_\lambda = \frac{1}{\Omega \mathcal{I}} \int j_\lambda A_{\rm eff}(\lambda) d\lambda, \qquad n(2\gamma) = \frac{\Delta\lambda_{\rm eq}}{\mathcal{I}} \int \lambda \frac{j_\lambda}{hc} A_{\rm eff}(\lambda) d\lambda \tag{A3}$$

where $\mathcal{I}$, the area-bandwidth product and $\Delta\lambda_{\rm eq}$, the equivalent width, are defined in Table 3. The unit for $n(2\gamma)$ (listed in Table 3) is count, resulting from our choice of 1 sr, an area of 1 $\rm cm^2$ and an integration time of 1 s. As can be seen from Table 3, each decay results in 0.27 photon in the FUV band and 0.44 photon in the NUV band. Consider an astronomical object emitting only via the two-photon process. Integrating over the pixels of this object's image, the ratio of FUV to NUV count rates is expected to be about 0.37. We end this section by noting Bracco et al. (2020) undertook a similar exercise but with a somewhat different approach. The two results agree to better than 10%.

B. EXCITATION OF H ATOMS IN 2S STATE

Recall that an H atom remains in the 2s state for a duration of A_{21}^{-1} or about 0.12 s. This is sufficiently long that over this period the atom could get perturbed or even further excited. The relevant processes are investigated below.

B.1. *Mixing of 2s-2p states by collisions*

The 2s $^2S_{1/2}$ state straddles $^2P_{1/2}$ (−1058 MHz; famous Lamb shift) and $^2P_{3/2}$ (+9911 MHz). Since the 2s state is metastable there was a hope that these fine-structure transitions could be observed in an astronomical setting, specifically the Sun (Wild 1952). The dipole elements connecting the 2s to the 2p levels are large. Purcell (1952) showed that distant encounters with protons are more effective than electrons (which had been studied in earlier literature) in changing the angular momenta of H atoms. The computed collisional coefficients are given in Table 4. The resulting modest critical density, $\approx 10^4\,\rm cm^{-3}$, significantly reduces the signal of the radio transitions from prime targets such the Sun or even HII regions (Dennison et al. 2005).

Table 4. Collisional Coefficients for H I $2s \to 2p$

transition	collider	q_0 ($\rm cm^3\,s^{-1}$)	γ
$2s\ ^2S_{1/2} \to 2p\ ^2P_{1/2}$	p^+	2.51×10^{-4}	−0.27
$2s\ ^2S_{1/2} \to 2p\ ^2P_{3/2}$	”	2.23×10^{-4}	−0.03
$2s\ ^2S_{1/2} \to 2p\ ^2P_{1/2}$	e^-	0.22×10^{-4}	−0.37
$2s\ ^2S_{1/2} \to 2p\ ^2P_{3/2}$	”	0.35×10^{-4}	−0.37

NOTE—Collisional coefficient at temperature $T = 10^4 T_4$ k is given by $q = q_0 T_4^\gamma$. Condensed from Osterbrock (1974).

B.2. *Excitation of 2s level by solar photons*

Bishop et al. (2001) mention in passing of the excitation of H atoms in 2s state by solar Balmer series photons. Here, we undertake a full investigation of this process and, in addition, consider bound-free ionization also.

[13] The tables for the effective area for FUV and NUV detectors were obtained from https://asd.gsfc.nasa.gov/archive/galex/tools/Resolution_Response/index.html

Excitation by Hα and Hβ (bound-bound). An H atom in the 2s $^2S_{1/2}$ state (level degeneracy, $g_l = 2$) can be excited by bound-bound process, for instance by absorption of a solar Hα photon. The excitation is then either to 3p $^2P_{1/2}$ ($g_u = 2$) or 3p $^2P_{3/2}$ level ($g_u = 4$). The oscillator strength, $f_{lu} \propto A_{ul} g_u/g_l$ (Equation 5), and so the total oscillator strength is the sum of the two oscillator strengths, $f_{2s\to 3p} = 0.4360$.

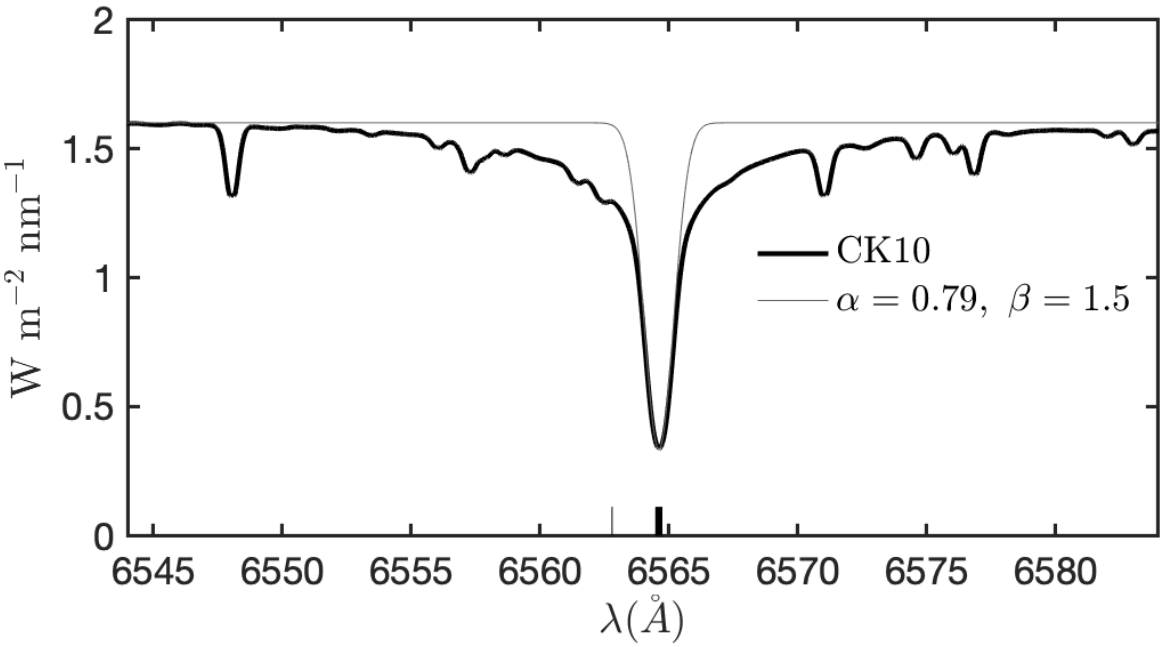

Figure 12. High-resolution spectrum of the Sun in the vicinity of Hα (data from Chance & Kurucz 2010). The absolute level at 6500 Å agrees to within a percent of the spectrum from SOLSPEC, aboard the International Space Station (Meftah et al. 2021). The dotted curve is a "chi-by-eye" fit restricted to the narrow Hα core. The model is given by $y(\lambda) = 1.6 \times [1 - \alpha \exp(-\beta x^2)]$ where $x = \lambda - \lambda(H\alpha)$, $\alpha = 0.79$ and $\beta = 1.5\,\text{Å}^{-2}$. The thick vertical stub is the vacuum wavelength, $\lambda(H\alpha) = 6564.614$ Å. The thin stub is the rest air wavelength of Hα (6562.801 Å), shown merely for reference.

The thermal velocity dispersion of H atoms is $\sigma_v = \sqrt{kT/m_H}$ or $2.9\,\text{km s}^{-1}$ for $T = 1,000$ K; here, m_H is the mass of an H atom. The corresponding FWHM is $\ln(256)^{1/2}\sigma_v \approx 6.8\,\text{km s}^{-1}$. We fit the solar H$\alpha$ absorption feature to a continuum+Gaussian absorption model (Figure 12) and derive an FWHM of $2\sqrt{\ln(2\alpha)/\beta} = 46\,\text{km s}^{-1}$. Since the geo-coronal H atoms have little Doppler shift with respect to the Sun we can assume that the flux of the solar Hα line is constant over the thermal frequency spread of an H atom. The Hα flux at the bottom of the absorption line is $0.34\,\text{W m}^{-2}\,\text{nm}^{-1}$ (Figure 12). This corresponds to $F_\lambda(0) = 1.1 \times 10^{13}\,\text{phot cm}^{-2}\,\text{s}^{-1}\,\text{Å}^{-1}$ or $F_\nu(0) = 158\,\text{phot cm}^{-2}\,\text{s}^{-1}\,\text{Hz}^{-1}$. Then the rate of H$\alpha$ pumping, per atom, is

$$\mathcal{R}_{H\alpha} = F_\nu(0)\frac{\pi e^2}{m_e c} f_{2s\to 3p} \approx 1.8 d_{\text{AU}}^{-2}\ \text{atom}^{-1}\,\text{s}^{-1} \tag{B4}$$

where d is the distance in AU. A similar exercise, carried out for solar Hβ absorption, yields

$$R_{H\beta} \approx 0.27 d_{\text{AU}}^{-2}\ \text{atom}^{-1}\,\text{s}^{-1}. \tag{B5}$$

The reduction is due to a smaller oscillator strength, $f_{2s\to 4p} = 0.1028$ and a slightly smaller solar spectral flux, $F(0) = 104\,\text{phot cm}^{-2}\,\text{s}^{-1}\,\text{Hz}^{-1}$.

Bound-free excitation. The bound-free absorption cross-section for frequency $h\nu > I_Z/n^2$ is given by

$$\sigma_{\text{bf}}(\nu) \approx 2.815 \times 10^{29} \frac{Z^4}{n^5 \nu^3} g_{\text{bf}}\,\text{cm}^2 \tag{B6}$$

where n is the energy quantum number of the excited H atom ($Z = 1$) and I_Z is the ionization potential (Gray 1992). The rate of bound-free pumping by solar continuum is

$$\mathcal{R}_{\text{bf}} = \int_{\nu_\alpha}^{\infty} \sigma_{\text{bf}} \frac{F(\nu)}{h\nu} d\nu = 0.12 d_{\text{AU}}^{-2}\ \text{atom}^{-1}\,\text{s}^{-1} \tag{B7}$$

where $F(\nu)$ is the solar irradiance supplied by SOLSPEC (see Figure 12) and $\nu_\alpha = I_H/4$ with $I_H = 13.6\,\mathrm{eV}$, the ionization potential of hydrogen. Incidentally, the resulting ionization rate is a tenth of ionization of H atoms by the Lyman continuum photons.

The overall rate of solar photonic excitation of 2s state is the sum of the rates given by Equation B4, B5 and and B7, $A_p = 2.2 d_{\mathrm{AU}}^{-2}\,\mathrm{atom\,s^{-1}}$. Solar optical pumping reduces the production of two-photon continuum by $A_{2\gamma}/(A_{2\gamma} + A_p)$.

C. THE THERMOSPHERE

The troposphere (0–12 km) contains most of the atmosphere. The temperature within the stratosphere (12–50 km) increases with height owing to absorption of solar UV by ozone. Once the ozone is dissociated temperature starts to decrease again with height until dissociation of oxygen and other molecules begins in the thermosphere. The mesosphere (50–85 km) is the layer between the stratosphere and the thermosphere. It is in this layer in which meteors burn, providing a convenient layer of Na I for laser guide-star adaptive astronomy.

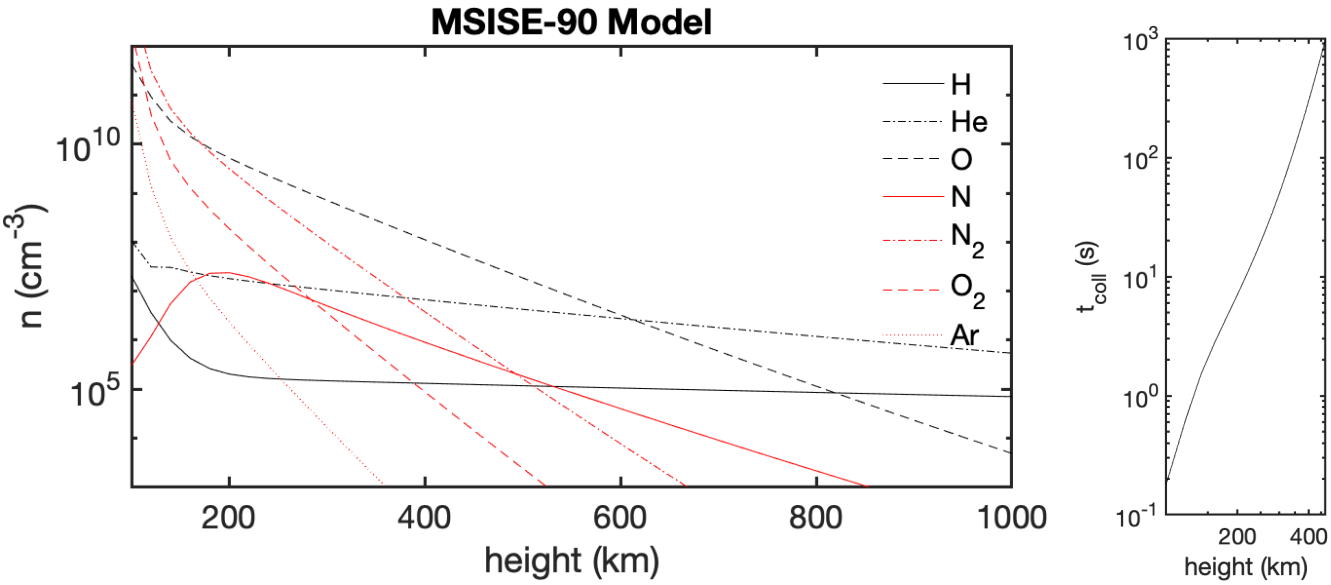

Figure 13. (Left) MSIS-E-90 atmosphere model for latitude of 30° and longitude of 0° on 01-January-2000 at a local time of 0100. From https://ccmc.gsfc.nasa.gov/modelweb/models/msis_vitmo.php (Right). The run, with height, of the mean time between collisions between an H atom and a neutral atom, $\tau = (\sigma_0 \sum_i n_i v_i)^{-1}$ where $\sigma_0 = 10^{-16}\,\mathrm{cm}^2$ is the characteristic "hard sphere" approximation for the cross section and n_i is the number density of species i and $v_i = \sqrt{3kT/m_H}$ is the relative velocity between H atom and species i.

The thermosphere (80 to about 700 km) is the region in which low-earth satellites are located (e.g., International Space Station: 420 km; HST 540 km; Swift Observatory: 550 km; *GALEX*: 685 km; FUSE, 750 km). The temperature in the thermosphere increases with height, owing to the absorption of solar EUV radiation by majority molecular species. Thus atoms are the primary constituents of the thermosphere. The temperature is strongly dependent on the solar EUV irradiance, ranging from 800 K to 2000 K (with strong day/night dependence). The radial extent of the thermosphere is quite sensitive to solar EUV, puffing up to 1000 km during solar maximum and receding to 500 km during solar minimum.

The density, ionization fraction and temperature of the thermosphere were obtained from the Community Coordinating Modeling Center (CCMC) portal[14]: MSIS-E-90 ("Mass Spectrometer and Incoherent Scatter radar - Exosphere-[19]90") for the run of neutral particles (Figure 13) and IRI-2016 (International Reference Ionosphere – 2016). Hydrogen is a minority species in the thermosphere and, furthermore, suffers from outflow. As such, Bishop et al. (2001) argue that the the hydrogen density profile in MSIS is not reliable.

[14] https://ccmc.gsfc.nasa.gov/about.php

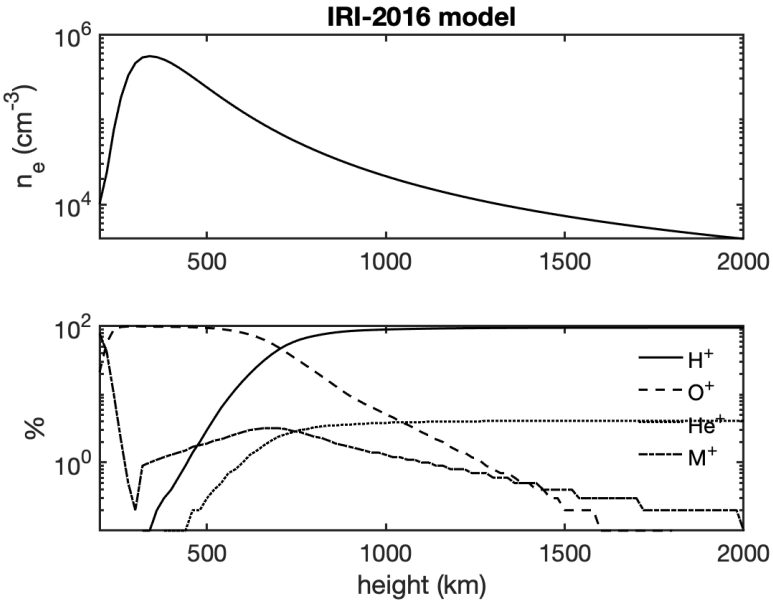

Figure 14. (Top) The run of electrons with altitude. (Bottom) The run of H^+, He^+, O^+ and other ions ("M^+": O_2^+, N^+ and NO^+), but expressed as a percentage of the electron density.

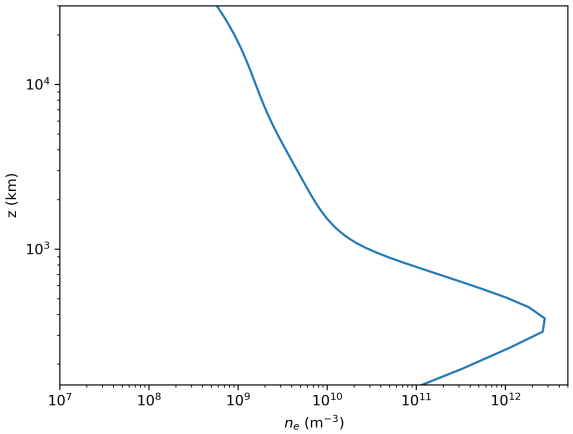

Figure 15. Radial profile of electrons (equatorial plane). Note the unit for electron density is m^{-3}. Figure supplied by Matthew D. Zettergren.

D. THE IONOSPHERE

As can be seen from Figure 14 the IRI-2016 model for electrons stops at 2,000 km. The higher altitude profile was generated, at my request, by Matthew Zettergren, Embry-Riddle Aeronautical University. The GEMINI open-source ionospheric model[15] was used in a 2-D meridional, dipole configuration to simulate plasma density evolution over several days (e.g., Zettergren & Snively 2015). The grid used covers ±60° in latitude, corresponding to apex altitudes of about 32,000 km (altitude of the model grid above magnetic equator). GEMINI solves conservation of mass, momentum, and energy equations for the ionospheric plasma for 6 ion species relevant to the terrestrial ionosphere, including protons. The model was run moderate for high solar and geomagnetic activity levels of F10.7=129.5, F10.7a=104.7, and solar index Ap=37. The date of the simulation is 10/6/2011 (near equinox) and the UT is about 5:45 (corresponding roughly to noon local time), representing a typical daytime plasma density state. Figure 15 shows a profile extracted from

[15] https://github.com/gemini3d

the geomagnetic equator. The results are meant to be illustrative of plasmasphere conditions during geomagnetically quiet times.

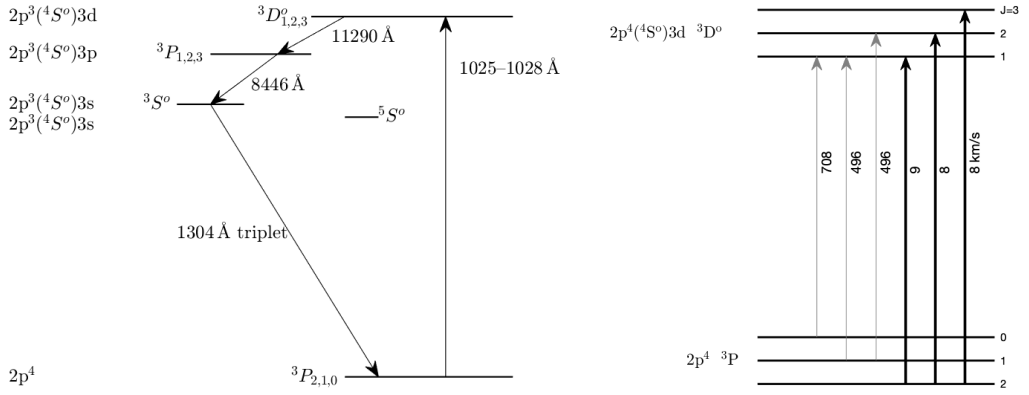

Figure 16. (*Left*). Partial Grotrian diagram for O I (to scale) displaying key allowed transtions. Solar Lyβ photons excite O I atoms from the ground state, $1s^2 2s^2 2p^4\ ^3P$, to the $1s^2 2s^2 2p^3(^4S^0)3d\ ^3D^o$ excited state. The O I atom can decay back to the ground state or decay to the $1s^2 s2^2 2p^3(^4S^o)3p\ ^3P$ state which then decays to ground state emitting, emitting along the way the famous O I 1304 Å triplet (composed of λ 1302.17 Å, λ 1304.86 Å, λ 1306.03 Å lines). The airglow O I] $\lambda\lambda$1355.56Å, 1358.51 Å is a spin-forbidden ($\Delta S \neq 0$; "inter-combination", "semi-forbidden") transition and results from electron excitation of O I from the ground state to the $2p^3(^4S^o)3s\ ^5S^o$ level (transition not marked by line). (*Right*): Grotrian diagram of O I (not to scale) restricted to the six allowed transitions between the ground state and $1s^2 2s^2 2p^3(^4S^0)3d\ ^3D^o$. The wavelength for each transition is converted to a velocity w.r.t. the rest wavelength of Lyβ. The rightmost three lines (thick black color) have sufficiently small velocity shifts, $\approx 9\,\mathrm{km\,s^{-1}}$, that they can be excited by solar Lyβ photons. These three lines are referred to as the "trio" in the main text. The remaining three (gray) lines have large velocity shifts, 500–700 $\mathrm{km\,s^{-1}}$, and so cannot be excited by solar Lyβ.

E. BOWEN FLUORESCENCE OF O I BY LYβ

The reason that the measurements in Table 1 are listed as Lyβ+OI is because there happens to be a near coincidence between Lyβ and an excited state of O I (Meier et al. 1987; see Figure 16 for a partial Grotrian diagram of O I). The atomic parameters for the resulting six transitions between the ground state and the excited state, $1s^2 2s^2 2p^3(^4S^o)3d\ ^3D^o$, are given in Table 5. Next, as can be gathered from Table 5, the excited OI atom has a probability of 71% to return to the ground state and 29% probability of decaying to the $1s^2 2s^2 2p^3(^4S^o)3p\ ^3P$ state with subsequent cascade to ground state with the last lap involving the famous O I λ1304 Å triplet. In addition to this channel, oxygen atoms in the thermosphere are directly excited by the solar chromospheric O I λ1304 Å triplet (in emission). Together, these two processes account for the brilliance of the airglow O I triplet. In contrast, the other FUV line of oxygen, O I] $\lambda\lambda$1356, 1358 Å, is weaker because it is spin-forbidden and is primarily excited by collisions with electrons.

F. THE EXOSPHERE

The exosphere is defined as the region in which the collisions of neutral particles with each other ceases to be important. The base of the exosphere ("exobase") depends on solar activity but a typical value is 500 km. Three families of particles are defined as follows: "ballistic" – particles that lack sufficient speed and so fall back; "escapers" – particles which have sufficient speed to escape; and "satellite" — particles which do undergo a rare collision ($R \lesssim 2.5\,R_E$) which sends them back down. Thus the particle density of the exosphere is not a simple power law. The temperature in the exosphere decreases to one third of the base value at $4\,R_E$ and two-fifth at $10\,R_E$; here, R_E is the radius of Earth ($\approx 6,400$ km). We adopt the "standard" temperature of 1025 K (cf. ØStgaard et al. 2003). The corresponding thermal rms velocity is $2.9\,\mathrm{km\,s^{-1}}$.

G. IMAGE & SOHO

G.1. *IMAGE*

IMAGE (Imager for Magnetopause-to-Aurora Global Exploration) was a NASA Medium Explorer class mission that was designed to study the response of Earth's magnetosphere to changes in the solar wind. It was launched into a

Table 5. Wavelength & Oscillator Strengths for selected O I levels

ind	λ(Å)	l	u	$A_{ul}(\mathrm{s}^{-1})$	f_{lu}	$E_l(\mathrm{cm}^{-1})$	$E_u(\mathrm{cm}^{-1})$
1	1025.762	$^3P_2$	$^3D^o_3$	7.66×10^7	0.0169	0	97 488.538
2	1025.763	$^3P_2$	$^3D^o_1$	2.11×10^6	2×10^{-4}	"	" 488.378
3	1025.763	$^3P_2$	$^3D^o_2$	1.91×10^7	0.0030	"	" 488.448
4	1027.431	$^3P_1$	$^3D^o_2$	5.71×10^7	0.0151	158.265	" 488.448
5	1027.431	$^3P_1$	$^3D^o_1$	3.17×10^7	0.0050	"	" 488.378
6	1028.157	$^3P_0$	$^3D^o_1$	4.22×10^7	0.0200	226.977	" 488.378
7	1,1286.34	$^3P_1$	$^3D^o_2$	2.32×10^7	0.2833	88 630.587	" 488.448
8	1,1286.40	$^3P_1$	$^3D^o_1$	1.29×10^7	0.2380	" 630.587	" 488.378
9	1,1286.91	$^3P_2$	$^3D^o_3$	3.09×10^7	0.1700	" 631.146	" 488.538
10	1,1287.02	$^3P_2$	$^3D^o_2$	7.74×10^6	0.1700	" 631.146	" 488.448
11	1,1287.11	$^3P_2$	$^3D^o_1$	8.60×10^5	0.1020	" 631.146	" 488.378
12	1,1283.72	$^3P_0$	$^3D^o_1$	1.72×10^7	0.5097	" 631.303	" 488.378
13	1302.168	$^3P_2$	$^3S^o_1$	3.41×10^8	0.0520	0	76 794.978
14	1304.858	$^3P_1$	$^3S^o_1$	2.03×10^8	0.0518	158.265	"
15	1306.029	$^3P_0$	$^3S^o_1$	6.67×10^7	0.0519	226.977	"

NOTE— "ind" stands for an internal index and u and l stand for upper and lower levels. For E_l and E_u '"' stands for adopting significant digits from the row above. The table has two sections separated by a horizontal line. For the top part, the lower level is the ground state, $1s^2 2s^2 2p^4\ ^3P_{2,1,0}$ and the upper level is the excited state $1s^2 2s^2 2p^3(^4S^o)3d\ ^3D_{1,2,3}$. For the lower part, the upper level is $1s^2 2s^2 2p^3(^4S^o)3p$ and the lower level is $1s^2 2s^2 2p^3(^4S^o)4s$. See also Figure 16. The atomic data are from https://physics.nist.gov/PhysRefData/ASD/lines_form.html.

highly elliptical orbit (1,000 km×46,000 km) with an inclination of 90.01° and an orbital period of about 14 hours. Its payload included an FUV imaging system which included the "GEO" photometer (Mende et al. 2000). The three photometers, oriented differently, respond to radiation coming from within their 1-degree FoV in the wavelength range 1150–1500 Å. This instrument was designed to measure the brightness of the geo-coronal Lyα. ØStgaard et al. (2003) provide a two-exponential model fit to the observed brightness. An example fit is

$$I(r) = 16.9 \exp(-r/1.03) + 1.06 \exp(-r/8.25)\,\mathrm{k}R \tag{G8}$$

where $I(r)$ is the Lyα intensity and the radius r is in units of R_E. Under the (admittedly simplistic) assumption of the medium being optically thin the authors invert the observations and provide density profile for H atoms.

G.2. *SWAN-SOHO*

The Solar & Heliospheric Observatory (SOHO) is a ESA-NASA mission that is located in the vicinity of the Earth-Sun L1 region and focused on the studies of the atmosphere of the Sun, the solar wind and helio-seismology. It carries Solar Wind ANistoropies (SWAN) instrument whose primary goal is to study the structure of the solar wind through its interaction with the IPM. A hydrogen cell acts by absorbing the incident solar light at the rest wavelength of Lyα. In effect, the cell provides a spectral resolution of 10^5 (Bertaux et al. 1995). SWAN data has also been used to study the distribution of geo-coronal H atoms (Baliukin et al. 2019).